

DETECTING 21 CM EOR SIGNAL USING DRIFT SCANS: CORRELATION OF TIME-ORDERED VISIBILITIES

AKASH KUMAR PATWA¹ AND SHIV SETHI¹

¹*Raman Research Institute, C. V. Raman Avenue, Sadashivanagar, Bengaluru 560080, India*

(Accepted October 23, 2019)

ABSTRACT

We present a formalism to extract the EoR HI power spectrum for drift scans using radio interferometers. Our main aim is to determine the coherence time scale of time-ordered visibilities. We compute the two-point correlation function of the HI visibilities measured at different times to address this question. We determine, for a given baseline, the decorrelation of the amplitude and the phase of this complex function. Our analysis uses primary beams of four ongoing and future interferometers—PAPER, MWA, HERA, and SKA1-Low. We identify physical processes responsible for the decorrelation of the HI signal and isolate their impact by making suitable analytic approximations. The decorrelation time scale of the amplitude of the correlation function lies in the range of 2–20 minutes for baselines of interest for the extraction of the HI signal. The phase of the correlation function can be made small after scaling out an appropriate term, which also causes the coherence time scale of the phase to be longer than the amplitude of the correlation function. We find that our results are insensitive to the input HI power spectrum and therefore they are directly applicable to the analysis of the drift scan data. We also apply our formalism to a set of point sources and statistically homogeneous diffuse correlated foregrounds. We find that point sources decorrelate on a time scale much shorter than the HI signal. This provides a novel mechanism to partially mitigate the foregrounds in a drift scan.

Keywords: cosmology: dark ages, reionization, first stars, cosmology: observations, cosmology: theory, methods: analytical, methods: statistical, techniques: interferometric

1. INTRODUCTION

The probe of the end of the cosmic dark age remains an outstanding issue in modern cosmology. From theoretical consideration, we expect the first luminous objects to appear at a redshift $z \simeq 30$. The radiation from these first light sources ionized and heated the neutral hydrogen (HI) in their neighbourhood. As the universe evolved, these ionized regions grew and merged, resulting in a fully ionized universe by $z \simeq 6$, as suggested by the measurement of Gunn-Peterson troughs of quasars (Fan et al. 2006). Recent Planck results on CMB temperature and polarization anisotropies fix the reionization epoch at $z \simeq 7.7$ (Planck Collaboration et al. 2018). The cosmic time between the formation of the first light sources ($z \simeq 30$, the era of cosmic dawn) and the universe becoming fully ionized ($z \simeq 6$) is generally referred to as the epoch of reionization (EoR). Many important astrophysical processes during this era, e.g. the growth and evolution of large scale structures and the nature of first light sources, can be best probed using the hyperfine transition of HI. Due to the expansion of the universe, this line redshifts to frequencies 70–200 MHz ($z \simeq 6$ –20), which can be detected using meter-wave radio telescopes.

Several existing and upcoming radio telescopes aim to detect the fluctuating component of this signal, e.g. radio interferometers—Murchison Widefield Array (MWA, Tingay et al. 2013, Bowman et al. 2013, Wayth et al. 2018), Low Frequency Array (LOFAR, van Haarlem et al. 2013), Donald C. Backer Precision Array for Probing the Epoch of Reionization (PAPER, Parsons et al. 2014), Hydrogen Epoch of Reionization Array (HERA, DeBoer et al. 2017), Giant Metrewave Radio Telescope (GMRT, Paciga et al. 2011). In addition there are multiple ongoing experiments to detect the global (sky-averaged) HI signal from this era—e.g. EDGES, SARAS (Bowman et al. 2018, Singh et al. 2018).

We focus on the fluctuating component of the HI signal in this paper. There are considerable difficulties in the detection of this signal. Theoretical studies suggest that the strength of this signal is of the order of 10 mK while the foregrounds are brighter than 100 K (for detailed review see Furlanetto et al. 2006, Morales & Wyithe 2010, Pritchard & Loeb 2012). These contaminants include diffuse galactic synchrotron, extragalactic point and extended radio sources, supernova remnants, free free emission, etc. Current experiments can reduce the thermal noise of the system to suitable levels in many hundred hours of integration. The foregrounds can potentially be mitigated by using the fact that the HI signal and its correlations emanate from the three-dimensional large scale structure at high redshifts. On the other hand, foreground contamination is dominated by spectrally smooth sources. This means that even if foregrounds can mimic the HI signal on the plane of the sky, the third axis, corresponding to the frequency, can be used to distinguish between the two. All ongoing experiments exploit this spectral distinction to isolate the HI signal from foreground contamination (e.g. Parsons & Backer 2009, Parsons et al. 2012).

Using data from ongoing experiments, many pipelines have been developed to analyze the signal (Paul et al. 2016, Paciga et al. 2011, Patil et al. 2017, Beardsley et al. 2016, Choudhuri et al. 2016, Trott et al. 2016, Dillon et al. 2015). PAPER (Ali et al. 2015) had placed the tightest constraint on the HI power spectrum but the result has since been retracted (Ali et al. 2018). Their revised upper limit is $(200 \text{ mK})^2$ at redshift $z = 8.37$ for $k \simeq 0.37 \text{ Mpc}^{-1}$ (Kolopanis et al. 2019). The current best upper limits on the HI power spectrum are: $(79.6 \text{ mK})^2$, $k \simeq 0.053h \text{ Mpc}^{-1}$, $z \simeq 10.1$ (LOFAR, Patil et al. 2017) and $(62.5 \text{ mK})^2$, $k = 0.2h \text{ Mpc}^{-1}$, $z \simeq 7$ (MWA, Barry et al. 2019). More recently, Bowman et al. (2018) reported the detection of an absorption trough of strength 500 mK in the global HI signal in the redshift range $15 < z < 19$.

Given the weakness of the HI signal, strong foregrounds, and the requirement of hundreds of hours of integration for detection, one needs extreme stability of the system, precise calibration, and reliable isolation of foregrounds. Drift scans constitute a powerful technique to achieve instrumental stability during an observational run. During such a scan the primary beam and other instrumental parameters remain unchanged while the sky intensity pattern changes. Two ongoing interferometers, PAPER and HERA, work predominantly in this mode while the others can also acquire data in this mode. Different variants of drift scans have been proposed in the literature: m -mode analysis (Shaw et al. (2014, 2015)), applied to OVRO-LWA data in Eastwood et al. (2018)), cross-correlation of the HI signal in time (Paul et al. 2014), drift and shift method (Trott 2014) and fringe-rate method (Parsons et al. (2016)), applied to PAPER data). Trott (2014) provided a framework to estimate the uncertainty in measurement of HI power spectrum based on visibility covariance. Using simulations of visibility covariance, Lanman & Pober (2019) have shown that the sample variance can increase up to 20% and 30% on the shortest redundant baselines of HERA and MWA respectively.

Owing to changing intensity pattern, it is conceptually harder to extract the HI signal from drift scans. As the HI signal is buried beneath instrumental noise, it is imperative that correct algorithm be applied to retain this sub-dominant component and prevent its loss (e.g. Cheng et al. (2018)).

In this paper, we extend the work of Paul et al. (2014) to delay space and, additionally, identify the effects of phase covariance and primary beam size. We also apply our formalism to foregrounds by considering a set of isotropically-distributed point sources and statistically homogeneous correlated diffuse emission. We work in both frequency and delay space, the preferred coordinate for separating foregrounds from the HI signal (e.g. Datta et al. 2010, Parsons et al. 2012). Our primary aim is to determine the correlation time scales of time-ordered visibilities of HI signal in drift scan observations. This information can be used to establish how the HI signal can be extracted from drift scans using correlation of visibilities measured at different times.

In the next section, we motivate the issue, develop our general formalism, and apply it to the HI signal in frequency and delay space. We use primary beams of PAPER, MWA, HERA, and SKA1-Low for our work. We discuss in detail analytic approximation of numerical results in the section and Appendix B. In section 3 we discuss the nature of foregrounds and compute the visibility correlation functions for a set of point sources and diffuse foregrounds. In section 4, we elaborate on how our formulation can be applied to drift scan data. We discuss many different approaches to the analysis of data including comparison with earlier attempts. In the final section, we summarize our main results.

Throughout this paper we use spatially-flat Λ CDM model with $H_0 = 100 h$ Km/sec/Mpc, $h = 0.67$, $\Omega_\Lambda = 0.6911$ (Planck Collaboration et al. 2016).

2. HI VISIBILITY CORRELATION IN DRIFT SCANS

The measured visibilities are a function of frequency, baseline, and time. The aim of this section is to determine the correlation structure of visibilities in these domains. In particular, our focus is on the correlation structure of visibilities as a function of time as the intensity pattern changes, for a fixed primary beam, during a drift scan.

This information allows us to average the data in the uv space with optimal signal-to-noise and prevent possible HI signal loss. The signal loss could occur if the data is averaged over scales larger than the scales of correlation (see e.g. Cheng et al. (2018)). For instance, the visibilities owing to HI signal are correlated for baselines separated by roughly the inverse of primary beam, so averaging data over pixels larger than the inverse of primary beam would result in the loss of HI signal. However, if the data is averaged using pixels much smaller than the correlation scale then it would result in sub-optimal signal-to-noise.

In this paper, we determine the time scales over which measured visibilities (for a given baseline, etc.) are coherent in time and therefore could be averaged in a drift scan to yield optimal signal-to-noise without any loss in HI signal. For this purpose, we derive the correlation function of visibilities, arising from the EoR HI signal, measured at two different times in a drift scan.

A pair of antennas of a radio interferometer measures the visibility V_ν , which is related to the sky intensity pattern as (Eq. 2.21 of Taylor et al. 1999):

$$V_\nu(u_\nu, v_\nu, w_\nu) = \int \frac{dl dm}{n} A_\nu(l, m) I_\nu(l, m) \exp[-2\pi i (u_\nu l + v_\nu m + w_\nu(n-1))] \quad (1)$$

Here ν is the observing frequency. (u_ν, v_ν, w_ν) are the components of the baseline vector between two antennas measured in units of wavelength. (l, m, n) define the direction cosine triplet in the sky with $n = \sqrt{1 - l^2 - m^2}$. $A_\nu(l, m)$ is the primary beam power pattern of an antenna element and $I_\nu(l, m)$ is the specific intensity pattern in the sky. We further define vectors $\mathbf{u}_\nu = (u_\nu, v_\nu)$ and $\boldsymbol{\theta} = (l, m)$. The intensity pattern owing to the EoR HI gas distribution $I_\nu(\boldsymbol{\theta})$ can be decomposed in mean and fluctuating components as:

$$I_\nu(\boldsymbol{\theta}) = \bar{I}_\nu + \Delta I_\nu(\boldsymbol{\theta}) \quad (2)$$

As an interferometer measures only fluctuating components of the signal, we can write:

$$V_\nu(\mathbf{u}_\nu, w_\nu) = \int \frac{d^2\theta}{n} A_\nu(\boldsymbol{\theta}) \Delta I_\nu(\boldsymbol{\theta}) \exp[-2\pi i (\mathbf{u}_\nu \cdot \boldsymbol{\theta} + w_\nu(n-1))] \quad (3)$$

The HI inhomogeneities $\delta_{\text{HI}}(\mathbf{k})$ arise from various factors such as HI density fluctuations, ionization inhomogeneities, etc. The fluctuation in the specific intensity $\Delta I_\nu(\boldsymbol{\theta})$ can be related to the HI density fluctuations in the Fourier space, $\delta_{\text{HI}}(\mathbf{k})$:

$$\Delta I_\nu(\boldsymbol{\theta}) = \bar{I}_\nu \int \frac{d^3k}{(2\pi)^3} \delta_{\text{HI}}(\mathbf{k}) \exp[i\mathbf{k} \cdot \mathbf{r}] \quad (4)$$

Here \mathbf{r} is the three-dimensional (comoving) position vector and its Fourier conjugate variable is \mathbf{k} ; k , the magnitude of the \mathbf{k} vector, is $k = |\mathbf{k}| = \sqrt{k_\perp^2 + k_\parallel^2} = \sqrt{k_{\perp 1}^2 + k_{\perp 2}^2 + k_\parallel^2}$, where \mathbf{k}_\perp and k_\parallel are the (comoving) components on the plane of the sky and along the line of sight, respectively. The position vector \mathbf{r} can be written in terms of the line of sight (parallel) and perpendicular components as $\mathbf{r} = r_\nu \hat{n} + r_\nu \boldsymbol{\theta}$; r_ν is the comoving distance. Eq. (4) reduces to:

$$\Delta I_\nu(\boldsymbol{\theta}) = \bar{I}_\nu \int \frac{d^3 k}{(2\pi)^3} \delta_{\text{HI}}(\mathbf{k}) \exp [ir_\nu (k_\parallel + \mathbf{k}_\perp \cdot \boldsymbol{\theta})] \quad (5)$$

As the HI fluctuations are statistically homogeneous, we can define the HI power spectrum $P_{\text{HI}}(k)$ as ¹:

$$\langle \delta_{\text{HI}}(\mathbf{k}) \delta_{\text{HI}}^*(\mathbf{k}') \rangle = (2\pi)^3 \delta^3(\mathbf{k} - \mathbf{k}') P_{\text{HI}}(k) \quad (6)$$

In tracking observations, the primary beam of the telescope follows a particular patch of the sky. In a drift scan, the sky pattern moves with respect to the fixed primary beam. This change of the sky intensity with respect to the fixed phase center introduces a time dependent phase $\boldsymbol{\vartheta}(t)$ in the expression of $\Delta I_\nu(\boldsymbol{\theta})$ in Eq. (5), which gives us the fluctuating component of the specific intensity as a function of time:

$$\Delta I_\nu(\boldsymbol{\theta}, t) = \bar{I}_\nu \int \frac{d^3 k}{(2\pi)^3} \delta_{\text{HI}}(\mathbf{k}) \exp [ir_\nu (k_\parallel + \mathbf{k}_\perp \cdot (\boldsymbol{\theta} - \boldsymbol{\vartheta}(t)))] \quad (7)$$

In Eq. (3) we use the expression of $\Delta I_\nu(\boldsymbol{\theta}, t)$ and expand terms containing n up to first non-zero order ² as $d^2\theta/n \simeq d^2\theta$ and $w_\nu(n-1) \simeq -(l^2 + m^2) w_\nu/2 = -\theta^2 w_\nu/2$. This gives us:

$$V_\nu(\mathbf{u}_\nu, w_\nu, t) \simeq \bar{I}_\nu \int \frac{d^3 k}{(2\pi)^3} \delta_{\text{HI}}(\mathbf{k}) \exp [ir_\nu k_\parallel] \int d^2\theta A_\nu(\boldsymbol{\theta}) \exp \left[-2\pi i \left(\left(\mathbf{u}_\nu - \frac{r_\nu}{2\pi} \mathbf{k}_\perp \right) \cdot \boldsymbol{\theta} + \frac{r_\nu}{2\pi} \mathbf{k}_\perp \cdot \boldsymbol{\vartheta}(t) - \frac{1}{2} w_\nu \theta^2 \right) \right]$$

Next we compute the two-point visibility correlation function between two different frequencies, baselines, and times:

$$\begin{aligned} & \langle V_\nu(\mathbf{u}_\nu, w_\nu, t) V_{\nu'}^*(\mathbf{u}'_{\nu'}, w'_{\nu'}, t') \rangle \\ & \simeq \bar{I}_\nu \bar{I}_{\nu'} \int \int \frac{d^3 k}{(2\pi)^3} \frac{d^3 k'}{(2\pi)^3} \langle \delta_{\text{HI}}(\mathbf{k}) \delta_{\text{HI}}^*(\mathbf{k}') \rangle \exp [i(r_\nu k_\parallel - r_{\nu'} k'_\parallel)] \int d^2\theta A_\nu(\boldsymbol{\theta}) \int d^2\theta' A_{\nu'}(\boldsymbol{\theta}') \\ & \times \exp \left[-2\pi i \left(\left(\mathbf{u}_\nu - \frac{r_\nu}{2\pi} \mathbf{k}_\perp \right) \cdot \boldsymbol{\theta} - \left(\mathbf{u}'_{\nu'} - \frac{r_{\nu'}}{2\pi} \mathbf{k}'_\perp \right) \cdot \boldsymbol{\theta}' + \frac{r_\nu}{2\pi} \mathbf{k}_\perp \cdot \boldsymbol{\vartheta}(t) - \frac{r_{\nu'}}{2\pi} \mathbf{k}'_\perp \cdot \boldsymbol{\vartheta}'(t') - \frac{1}{2} w_\nu \theta^2 + \frac{1}{2} w'_{\nu'} \theta'^2 \right) \right] \end{aligned} \quad (8)$$

Using Eq. (6) in Eq. (8) gives the two-point correlation function in terms of the HI power spectrum $P_{\text{HI}}(k)$. We first note that the time dependence of Eq. (8) occurs as the time difference, Δt in just one term $\boldsymbol{\vartheta}'(t') - \boldsymbol{\vartheta}(t) = \Delta \boldsymbol{\vartheta}(\Delta t)$ which is obtained by dropping the frequency dependence of r_ν . This approximation is discussed in detail in the next subsection. Eq. (A4) is used to express the time-dependent part of the correlation function explicitly in terms of change in the hour angle ΔH (for details see Appendix A). This gives us:

$$\begin{aligned} & \langle V_\nu(\mathbf{u}_\nu, w_\nu, t) V_{\nu'}^*(\mathbf{u}'_{\nu'}, w'_{\nu'}, t') \rangle = \bar{I}_\nu \bar{I}_{\nu'} \int \frac{d^3 k}{(2\pi)^3} P_{\text{HI}}(k) \exp [ik_\parallel (r_\nu - r_{\nu'})] \exp [ir_\nu k_{\perp 1} \cos \phi \Delta H] \\ & \times Q_\nu(\mathbf{k}_\perp, \mathbf{u}_\nu, w_\nu, \Delta H = 0) Q_{\nu'}^*(\mathbf{k}_\perp, \mathbf{u}'_{\nu'}, w'_{\nu'}, \Delta H) \end{aligned} \quad (9)$$

Here ϕ is the latitude of the telescope and the Fourier beam (or 2D Q -integral) is defined as:

$$Q_\nu(\mathbf{k}_\perp, \mathbf{u}_\nu, w_\nu, \Delta H) = \int d^2\theta A_\nu(\boldsymbol{\theta}) \exp \left[-2\pi i \left(\mathbf{x}_u \cdot \boldsymbol{\theta} - \frac{1}{2} y \theta^2 \right) \right] \quad (10)$$

$$\text{with} \quad x_u = u_\nu - \frac{r_\nu}{2\pi} (k_{\perp 1} + k_{\perp 2} \sin \phi \Delta H) \quad (11)$$

$$x_v = v_\nu - \frac{r_\nu}{2\pi} (k_{\perp 2} - k_{\perp 1} \sin \phi \Delta H) \quad (12)$$

$$y = w_\nu + \frac{r_\nu}{2\pi} k_{\perp 1} \cos \phi \Delta H \quad (13)$$

¹ We also assume here that the HI signal is statistically isotropic which allows us to write the power spectrum as a function of $|\mathbf{k}|$. Statistical isotropy is broken owing to line of sight effects such as redshift space distortion and line-cone anisotropies, which would make the power spectrum depend on the angle between \mathbf{k} and the line of sight.

² As discussed below, we use primary beams corresponding for many ongoing and future radio telescopes for our analysis. For all the cases, this approximation holds for the main lobe of the primary beam, which means, as we show later, that our main results are unaffected.

In this paper we consider only the zenith drift scan. Non-zenith drift scans can be treated by replacing ϕ with $\phi + \chi$, where χ is the angle between the latitude of the zenith and the phase center of the observed field (for details see Appendix A in Paul et al. 2014). This doesn't impact our main results. Eq. (9) can be numerically solved for a given primary beam pattern $A_\nu(\theta)$. We next discuss the visibility correlation in delay space, the preferred coordinate for analysing the data.

2.1. Visibility Correlation in Delay Space

To compute the HI visibility correlation function in delay space (τ) we define:

$$V_\tau(\mathbf{u}_0, w_0, t) = \int_{\nu_0 - B/2}^{\nu_0 + B/2} d\nu V_\nu(\mathbf{u}_\nu, w_\nu, t) \exp[2\pi i \tau \nu] \quad (14)$$

Throughout this paper the subscript '0' under any variable denotes the value of that variable at the central frequency. Throughout this paper, we use: $\nu_0 \simeq 154$ MHz and bandpass $B \simeq 10$ MHz. Its cross-correlation in delay space can be expressed as:

$$\langle V_\tau(\mathbf{u}_0, w_0, t) V_\tau^*(\mathbf{u}'_0, w'_0, t') \rangle = \iint_{\nu_0 - B/2}^{\nu_0 + B/2} d\nu d\nu' \langle V_\nu(\mathbf{u}_\nu, w_\nu, t) V_{\nu'}^*(\mathbf{u}'_{\nu'}, w'_{\nu'}, t') \rangle e^{-2\pi i \tau \Delta\nu} \quad (15)$$

Eq. (15) can be reduced to a more tractable form by making appropriate approximations. We expand frequency-dependent variables in exponents around ν_0 up to the first order. Thus $(r_\nu - r_{\nu'}) \simeq -\dot{r}_0 \Delta\nu$, denoting $(dr_\nu/d\nu)_{\nu_0} = \dot{r}_0$, $\nu' - \nu = \Delta\nu$. To the same order, the approximation made following Eq. (9) is also valid. We further approximate $\mathbf{u}_\nu \simeq \mathbf{u}_0$ and drop the weak frequency dependence of the mean specific intensity and primary beam within the observing band-width B . We discuss the impact of these approximations in section 2.2. This gives us:

$$\begin{aligned} \langle V_\tau(\mathbf{u}_0, w_0, t) V_\tau^*(\mathbf{u}'_0, w'_0, t') \rangle &= \bar{I}_0^2 \int \frac{d^3 k}{(2\pi)^3} P_{\text{HI}}(k) \exp[i r_0 k_{\perp 1} \cos \phi \Delta H] \left(\iint_{\nu_0 - B/2}^{\nu_0 + B/2} d\nu d\nu' \exp[-i \Delta\nu (k_{\parallel} \dot{r}_0 + 2\pi\tau)] \right) \\ &\times Q_{\nu_0}(\mathbf{k}_{\perp}, \mathbf{u}_0, w_0, \Delta H = 0) Q_{\nu_0}^*(\mathbf{k}_{\perp}, \mathbf{u}'_0, w'_0, \Delta H) \end{aligned} \quad (16)$$

The integrals over ν and ν' can be solved in two ways. They can be solved by changing the variables from (ν, ν') to (x, y) . $x = \nu' - \nu = \Delta\nu$ and $y = (\nu' + \nu)/2$. They can also be solved by separating $\Delta\nu = \nu' - \nu$ and integrating over ν and ν' individually. The resulting function peaks sharply at $\tau = -\dot{r}_0 k_{\parallel}/(2\pi)$. The major contribution to the integral in Eq. (16) occurs when $k_{\parallel} = -2\pi\tau/\dot{r}_0$, which gives us the well-known correlation scale along the line-of-sight direction (e.g. Paul et al. 2016). We use the δ -function approximation for frequency integrals:

$$\iint_{\nu_0 - B/2}^{\nu_0 + B/2} d\nu d\nu' \exp[-i \Delta\nu (k_{\parallel} \dot{r}_0 + 2\pi\tau)] = B^2 \text{sinc}^2 \left[\pi B \left(\tau + \frac{\dot{r}_0}{2\pi} k_{\parallel} \right) \right] \simeq \frac{2\pi B}{|\dot{r}_0|} \delta \left(k_{\parallel} - \frac{2\pi\tau}{|\dot{r}_0|} \right) \quad (17)$$

This approximation preserves the area under the curve. We note that the delta function approximation used in Eq. (17) could break down if B is small. For $B = 10$ MHz, we use in the paper, it is an excellent assumption. For a much smaller B , the sinc function in the equation can be directly integrated without making any difference to our main results. We denote $\dot{r}_0 = -|\dot{r}_0|$ because the comoving distance decreases with increasing frequency. Using this in Eq. (16) we find, with $k_{\parallel} = 2\pi\tau/|\dot{r}_0|$:

$$\begin{aligned} \langle V_\tau(\mathbf{u}_0, w_0, t) V_\tau^*(\mathbf{u}'_0, w'_0, t') \rangle &\simeq \bar{I}_0^2 \frac{B}{|\dot{r}_0|} \int \frac{d^2 k_{\perp}}{(2\pi)^2} P_{\text{HI}}(k) \exp[i r_0 k_{\perp 1} \cos \phi \Delta H] \\ &\times Q_{\nu_0}(\mathbf{k}_{\perp}, \mathbf{u}_0, w_0, \Delta H = 0) Q_{\nu_0}^*(\mathbf{k}_{\perp}, \mathbf{u}'_0, w'_0, \Delta H) \end{aligned} \quad (18)$$

Here $k = \sqrt{k_{\perp 1}^2 + k_{\perp 2}^2 + (2\pi\tau/|\dot{r}_0|)^2}$. Eq. (18) generalizes the results of Paul et al. (2014) to delay space and also accounts for the impact of the w -term. To further simplify Eq. (18) we need an expression for the primary beam pattern. We consider four radio interferometers in our analysis.

MWA: MWA has square-shaped antennas called tiles. Each tile consists of 16 dipoles placed on a mesh and arranged in a 4x4 grid at spacing of roughly 1.1 meters. Effective area of a tile $A_{\text{eff}} = 21.5 \text{ m}^2$ at 150 MHz (Tingay et al.

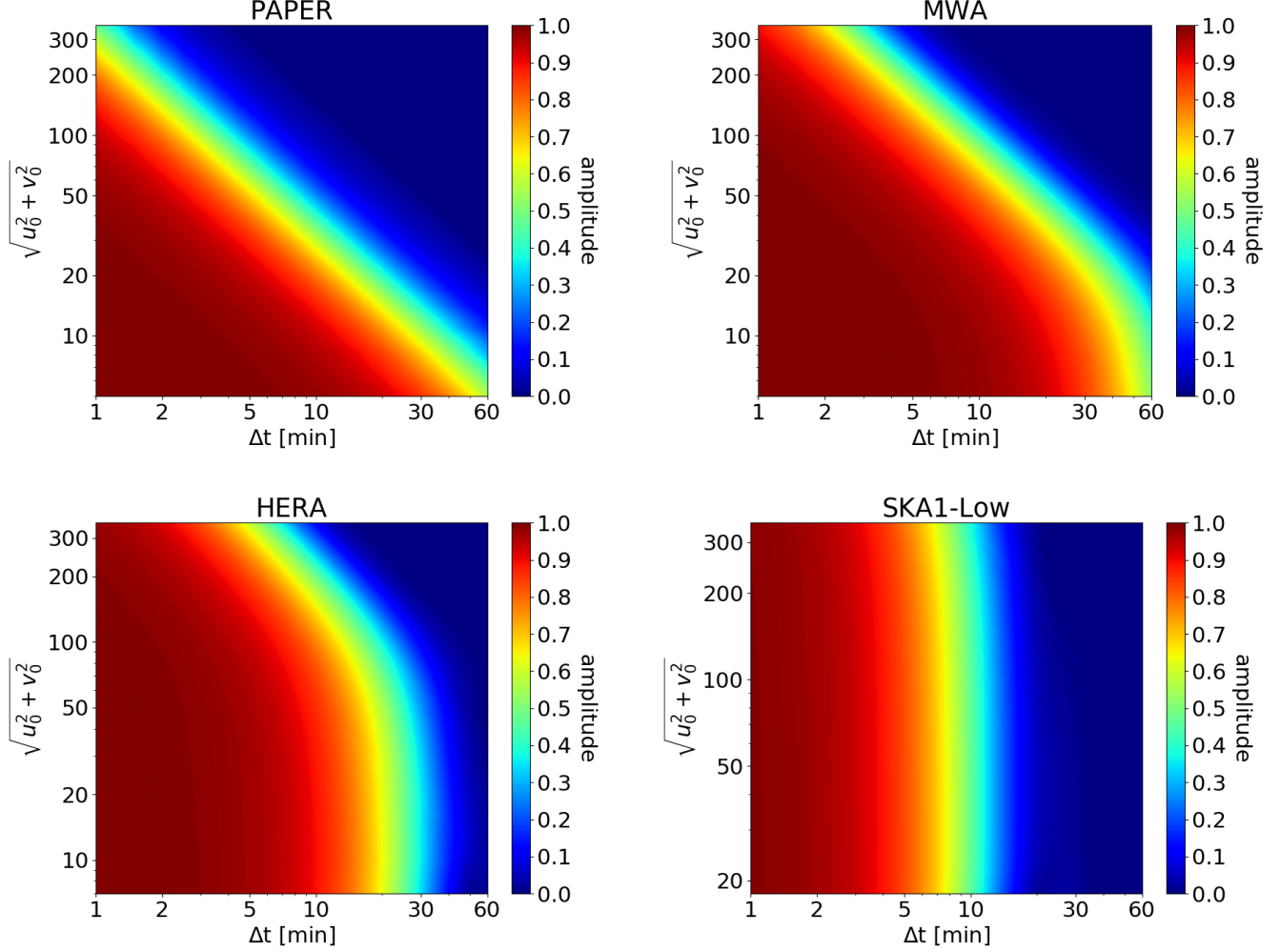


Figure 1. The figure displays the amplitude of the visibility correlation function as a function of Δt , normalized to unity for $\Delta t = 0$. The quantity plotted in the figure is $\langle V_\tau(\mathbf{u}_0, w_0, t) V_\tau^*(\mathbf{u}_0, w_0, t') \rangle / \langle V_\tau(\mathbf{u}_0, w_0, t) V_\tau^*(\mathbf{u}_0, w_0, t) \rangle$ as a function of baseline length $|\mathbf{u}_0| = \sqrt{u_0^2 + v_0^2}$ and $\Delta t = t' - t$, for $u_0 = v_0, w_0 = 0$, and $\tau = 0$. The amplitude of the correlation function decorrelates mainly due to the rotation of the intensity pattern. However the impact of the traversal of the intensity pattern becomes important for smaller primary beams on small baselines. As seen in the figure, for all baselines for PAPER and large baselines for MWA, HERA, and SKA1-Low, the decorrelation time scales are proportional to $1/|\mathbf{u}_0|$ and $1/\sqrt{\Omega}$. This effect is discussed in subsection 2.1.1 (point (b)). On smaller baselines in MWA, HERA, and SKA1-Low panels, the traversal of the intensity pattern starts dominating the decorrelation. This effect is discussed in subsection 2.1.1 (point (a)).

2013). The square of the absolute value of the 2D Fourier transform of the antenna shape gives the antenna power response. For MWA $A_\nu(l, m) = \text{sinc}^2(\pi L_\nu l) \text{sinc}^2(\pi L_\nu m)$. Here $L_\nu = L(\nu/\nu_0)$; $L (\equiv \sqrt{A_{\text{eff}}}/\lambda_0 \simeq 2.4)$ is the length of the square tile in units of central wavelength ($\lambda_0 \simeq 1.95\text{m}$). Therefore, the 2D primary beam response $A_\nu(l, m)$ can be represented as a product of two independent 1D patterns; $A_\nu(l, m) = A_\nu(l)A_\nu(m)$.

PAPER, HERA and SKA1-Low: Individual element in PAPER, HERA, and SKA1-Low correspond to dishes of diameter 2 meters, 14 meters, and 35 meters, respectively. The beam pattern at a frequency ν can be expressed as: $A_\nu = 4|j_1(\pi d_\nu \sqrt{l^2 + m^2}) / (\pi d_\nu \sqrt{l^2 + m^2})|^2$, where $j_1(x)$ is the spherical Bessel function and d_ν is the diameter of the dish in the units of wavelength. Unlike MWA, this primary beam pattern is not separable in l and m . Or the double integral over angles in Eq. (10) cannot be expressed as a product of two separate integrals over l and m . We do not

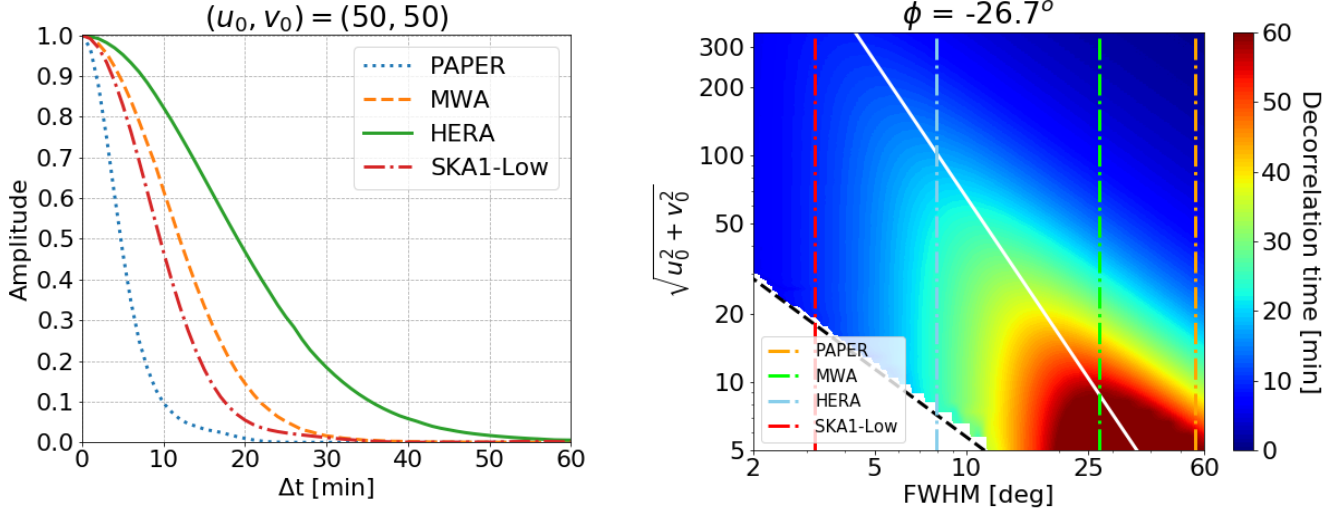


Figure 2. Left Panel: The amplitude of the visibility correlation function is shown as a function of Δt for a fixed baseline for different primary beams. Right Panel: The isocontours of the decorrelation time are shown in the primary beam–baseline plane; the decorrelation time is defined as Δt such that the amplitude of correlation function falls to half its value as compared to $\Delta t = 0$. The Figure assumes Gaussian beams (Eq. 20) with $\text{FWHM} = 2\sqrt{\log_e(2)\Omega_{0g}}$. The region on the left bottom is excluded because the shortest baseline $\sqrt{u_0^2 + v_0^2} = d_0$, where d_0 is the primary element of the telescope in units of the central wavelength, λ_0 . There could be minor differences between this figure and Figure 1 because we use a fixed telescope latitude $\phi = -26.7^\circ$ for all primary beams. The primary beams of the four interferometers studied in this paper are marked on the figure. The White line demarcates the regions dominated by rotation (above the line) and traversal of intensity pattern (for further discussion see the text).

consider LOFAR in our analysis as its core primary beam, suitable for EoR studies, is close to SKA1-Low³. For MWA and SKA1-Low: $\phi = -26.7^\circ$ and for HERA and PAPER: $\phi = -30.7^\circ$.

In Figure 1 we show the amplitude of the correlation function (Eq. (18)), normalized to unity for $\Delta t = 0$, as a function of the time difference, $\Delta t \equiv t' - t$ in a drift scan. In the Figure, we use the HI power spectrum $P_{\text{HI}}(k)$ given by the simulation of Furlanetto et al. (2006); we discuss the dependence of our results on the input power spectrum below in subsection 2.2.1. The figure displays numerical results for different primary beams as a function of baselines length $|\mathbf{u}_0| = \sqrt{u_0^2 + v_0^2}$, for $w_0 = 0$ and $\tau = 0$. Our numerical results further show that the visibility correlation function in time domain is nearly independent of τ . This is discussed and justified in Appendix B using analytic approximations. Figure 2 complements Figure 1 and allows us to study the change in decorrelation time when the primary beam is changed for a fixed baseline; it will be discussed in detail in the next sub-section.

To get analytic insights into the nature of numerical results displayed in Figures 1 and 2, we consider a separable and symmetric Gaussian beam.

2.1.1. Fourier Beam and HI Correlation with Gaussian Beam

The Fourier Beam introduced in Eq. (10) is the response of the primary beam in the Fourier domain. It has two useful properties which makes the computation of the Fourier beam easier. If the primary beam is separable, $A_\nu(l, m) = A_\nu(l)A_\nu(m)$, then the Fourier beam is also separable, $Q_\nu(\mathbf{u}_\nu) = Q_\nu^1(u_\nu)Q_\nu^2(v_\nu)$. And if the 1D primary beam response, $A_\nu(l)$, is an even function then the 1D Fourier beam, $Q_\nu^1(u_\nu)$, satisfies the following relations.

$$\begin{aligned} Q_\nu^1(-x_u, y) &= Q_\nu^1(x_u, y) \\ Q_\nu^1(x_u, -y) &= Q_\nu^{1*}(x_u, y) \end{aligned} \quad (19)$$

The expressions above are also valid for $Q_\nu^2(v_\nu)$. This shows that it is sufficient to calculate Fourier beam for only $x_u, y \geq 0$. The variables x_u, x_v , and y are defined in Eqs. (11)–(13). x_u and x_v determine the correlation scales in the

³ <http://old.astron.nl/radio-observatory/astronomers/lofar-imaging-capabilities-sensitivity/lofar-imaging-capabilities/lofa>

neighbourhood of the Fourier mode, $2\pi\mathbf{u}_0/r_0$, at which the Q -integral receives maximum contribution. The variable y can be viewed as an effective w -term. We note that when y is small $Q_\nu^1(x_u, y)$ is large but falls very rapidly along x_u . For larger values of y , $Q_\nu^1(x_u, y)$ is smaller and goes to zero slowly along x_u . This behaviour can be understood as follows: the effective beam size shrinks for larger value of w -term, resulting in a decrease in signal strength but an increase in the correlation scale (e.g. Paul et al. 2016; Cornwell et al. 2008).

The discussion also applies to 2D Fourier beams. The 2D Fourier beam is a function of Fourier coordinates x_u, x_v and parameter y . The point $(x_u, x_v) = (0, 0)$ receives the maximum contribution and picks out Fourier modes, $k_{\perp 1}, k_{\perp 2}$. Large beams have smaller Fourier beams e.g. for PAPER the Fourier beam is the smallest of all the cases we consider. The width of the Fourier beam decides the range of correlation scales of the HI signal. This range is roughly on the order of $2/\sqrt{\Omega} \simeq 2d$ where Ω is the primary beam solid angle and d is the antenna size in the units of wavelength. The amplitude of the Fourier beam is more sensitive to y if the beam is larger (PAPER, MWA).

To gain further analytic insights into the HI correlation function, we use a Gaussian primary beam in our formalism to compute the Fourier beam. For illustration, we choose Gaussian primary beam of solid angle Ω_{0g} at $\nu_0 = 154.24$ MHz ($\Omega_{0g} = 0.25/L^2$ roughly matches the MWA primary beam). This gives us:

$$A_{\nu_0}(l, m) = e^{-(l^2+m^2)/\Omega_{0g}} \quad (20)$$

To compute the Fourier response of a Gaussian beam analytically, we extend the limits of the integral from $[-1, 1]$ to $[-\infty, \infty]$, which is a valid procedure as the integrand falls rapidly outside the support of the primary beam. Using Eq. (10), we obtain:

$$Q_{\nu_0}(\mathbf{k}_\perp, \mathbf{u}_0, w_0, \Delta H) = \frac{\pi\Omega_{0g}}{1 - i\pi y\Omega_{0g}} \exp \left[-\frac{\pi^2\Omega_{0g}(x_u^2 + x_v^2)}{1 - i\pi y\Omega_{0g}} \right] \quad (21)$$

We assume $\mathbf{u}_0 = \mathbf{u}'_0$ and $\mathbf{k}_\perp = (2\pi/r_0)\mathbf{u}_0$ to study the time behaviour of the correlation function relevant in a drift scan. The time-dependent part of the visibility correlation function is determined by the product of two Fourier beams separated by drift time ΔH in Eq. (18). For Gaussian beam this product is:

$$Q_{\nu_0}(\Delta H = 0)Q_{\nu_0}^*(\Delta H) = \frac{(\pi\Omega_{0g})^2}{(1 - i\pi\Omega_{0g}w_0)(1 + i\pi\Omega_{0g}y)} \exp \left[-\frac{\pi^2\Omega_{0g}|\mathbf{u}_0|^2 \sin^2 \phi \Delta H^2}{1 - i\pi y\Omega_{0g}} \right] \quad (22)$$

where only the dependence on the time variable is retained in the LHS for brevity. As discussed above, $y = (w'_0 + u_0 \cos \phi \Delta H)$ acts as an effective w -term. For a zenith drift scan we study in this paper, the w -term is small, so we put $w_0 = w'_0 = 0$. We find the amplitude of the product of the Fourier beams to be:

$$|Q_{\nu_0}(\Delta H = 0)Q_{\nu_0}^*(\Delta H)| = \frac{(\pi\Omega_{0g})^2}{\sqrt{(1 + \pi^2\Omega_{0g}^2 u_0^2 \cos^2 \phi \Delta H^2)}} \exp \left[-\frac{\pi^2\Omega_{0g}|\mathbf{u}_0|^2 \sin^2 \phi \Delta H^2}{1 + \pi^2\Omega_{0g}^2 u_0^2 \cos^2 \phi \Delta H^2} \right] \quad (23)$$

Eq. (23), along with Eqs. (18) and (22), allows us to read off several salient features of the visibility correlation function in a drift scan.

Due to the rotation of the earth on its axis, the sources in the sky move with respect to the fixed phase center ($l = 0, m = 0$) of a telescope located at latitude ϕ . The changing intensity pattern is a combination of two motions: rotation around a fixed phase center and the east-west translation of the pattern with respect to the fixed phase center (Eq. (A2)). In Fourier space, the rotation causes a time-dependent mixing of Fourier modes in the plane of the sky, while the translation introduces a new time-dependent phase which is proportional to $k_{\perp 1}$, the component of the Fourier mode in the east-west direction (Eq. (A4)). In addition to these two effects, which are linear in the angle, we also retain a second order term which becomes important for large beams (Eqs. (A2) and (A4)). The impact of each of these effects on the visibility correlation function is discussed next:

- (a) *Traversal time of coherence scale:* The phase term proportional to $\exp(ir_0 k_{\perp 1} \cos \phi \Delta H)$ in Eq. (18) represents this effect. $\Delta H \simeq 1/(r_0 k_{\perp 1} \cos \phi)$ is the time over which a coherent feature of linear size $1/k_{\perp 1}$ is traversed in the east-west direction. As $r_0 k_{\perp 1} \simeq 2\pi u_0$, $\Delta H \simeq 1/(2\pi u_0 \cos \phi)$ appears to give a rough estimate of the time over which the decorrelation occurs for a given u_0 , the east-west component of the baseline. However, it doesn't give a reasonable estimate for the decorrelation time scale of the amplitude of the correlation function

as Eq. (18) can be multiplied and divided by $\exp(i2\pi u_0 \cos \phi \Delta H)$ which allows us to absorb the fastest changing term as the phase term of the correlation function. The correlation time scale of the amplitude of the correlation function depends on the slow phase $\exp(i(r_0 k_{\perp 1} - 2\pi u_0) \cos \phi \Delta H)$ whose contribution to the visibility correlation is determined by the primary beam as we discuss below.

- (b) *Rotation of intensity pattern*: This effect is captured by the numerator in the Gaussian in Eq. (23), which shows that the decorrelation owing to the rotation of the intensity pattern is proportional to $1/(\Omega_{0g}^{1/2} |\mathbf{u}_0| |\sin \phi|)$. This effect, unlike (a), depends the magnitude of the baseline and not its east-west component. Eqs. (10)–(12), along with Eq. (A2) and Eq. (A4), allow us to understand this effect. When visibilities at two times are correlated for a given baseline, they respond to different Fourier modes of the HI power spectrum owing to the rotation of intensity pattern in a drift scan (Eqs. (10)–(12)). The extent of correlation of visibilities which get contribution from different Fourier modes depends on the primary beam: the smaller the primary beam the larger is the range of Fourier modes that contribute to the correlation. Therefore, the decorrelation time is proportional to $\Omega_{0g}^{-1/2}$.
- (c) *Large field of view*: The terms proportional to Ω_{0g}^2 in Eq. (23) (or more generally the terms proportional to y in Eq. (21)) are responsible for this effect. These terms correspond to an effective w -term, a part of which arises from w_0 and the remaining is the higher-order time-dependent phase in a drift scan. This effect is important when the primary beam or w_0 is large.⁴

We next discuss the relative importance of (a), (b), and (c) in understanding Figures 1 and 2. We first note that (c) doesn't play an important role in explaining qualitative features seen in the Figures. Its impact is only mildly important for PAPER at the smallest baselines we consider.

For PAPER, the decorrelation time in the Figure scales linearly as the inverse of the length of the baseline $1/|\mathbf{u}_0|$. Figure 1 shows only the case $u_0 = v_0$. We have checked that the behaviour seen in the figure is nearly independent of the individual components of the baseline. Also a comparison of decorrelation times between PAPER and MWA shows that the decorrelation times scale as $\Omega_{0g}^{-1/2}$ for baseline $|\mathbf{u}_0| \gtrsim 25$. A comparison of these two cases with large baselines $|\mathbf{u}_0| \gtrsim 150$ for HERA and SKA1-Low also shows the same scaling with the primary beam. This means that (b) is the dominant decorrelation mechanism in all these cases.

For short baselines for MWA, HERA, and SKA1-Low the behaviour is markedly different. If (b) alone determined the decorrelation in these cases, the decorrelation time would be longer as the primary beam is smaller in these two cases, but this behaviour is seen only for longer baselines. Therefore, (a) plays an important role in these cases. For large primary beams, (a) is unimportant because the slow phase discussed above is closer to zero, as it gets contribution from a small range of Fourier modes. However, for narrower primary beams, this term gets contribution from a larger range of Fourier modes which results in cancellation when integration over $k_{\perp 1}$ is carried out. This results in a reduction of correlation time scale. This effect is more dominant for smaller baselines for the following reason: for a given u_0 , the range of Fourier modes that contribute to the visibility correlation function is $\Delta k_{\perp 1} \simeq 1/(r_0 \Omega_{0g}^{1/2})$ (i.e. size of the Fourier beam) centered around $k_{\perp 1} = 2\pi u_0/r_0$ (e.g. Eqs. (10)–(12)). It should be noted that $\Delta k_{\perp 1}$ is only determined by the size of the primary beam while $k_{\perp 1}$ scales with the east-west component of the baseline. This implies that for long baselines, $k_{\perp 1} \gg \Delta k_{\perp 1}$. In this case, the visibility correlation function is dominated by the contribution of a single Fourier mode, which suppresses the impact of possible cancellation that occurs owing to the mixing of Fourier modes, diminishing the impact of (a) for long baselines. However, when $\Delta k_{\perp 1} \simeq k_{\perp 1}$, the effect becomes important and it determines the decorrelation time scale for shorter baselines.

For small baselines and narrower primary beams, both (a) and (b) play an important role so it is worthwhile to investigate the dependence of the decorrelation time on the components of baselines (Figure 1 assumes $u_0 = v_0$). We have checked many different combinations of u_0 and v_0 and find that the qualitative features of Figure 1 are largely determined by the the length of the baseline. But, as discussed below, the phase of the correlation function is dominated by the east-west component of the baseline.

The correlation structure in the primary-beam- Δt -baseline space is further explored in Figure 2. In the left panel, we show the amplitude of the correlation function as a function of Δt for a fixed baseline for different primary beams.

⁴ Throughout our analysis we assume $w_0 = 0$ and we only consider the impact of the time-dependent term. Our assumption would be valid for a zenith drift scan, which we assume, for a near-coplanar interferometric array. Coplanarity is generally a good assumption as our focus for the detection of the HI signal is short baselines, e.g. for MWA $w_0 \ll |\mathbf{u}|$ for a zenith scan. We can gauge the quantitative impact of non-zero w_0 using Eq. (22). The main effect of non-zero w_0 is to yield a smaller effective primary beam (Paul et al. (2016, 2014); Cornwell et al. (2008)) and to introduce additional phase in the visibility correlation function (Eq. (B8)).

The right panel shows the isocontours of the decorrelation time in the primary beam–baseline plane; the decorrelation time is defined as the time difference Δt at which the amplitude of the correlation function falls to half its value at $\Delta t = 0$. For each baseline, the decorrelation time reaches a maximum value as a function of the primary beam. Our formalism allows us to understand this general behaviour: for smaller primary beam, the Fourier beam is large which causes decorrelation owing to mode-mixing in the transverse motion of the intensity pattern (point (a)). For larger primary beam, the rotation of intensity pattern is responsible for the decorrelation (point (b)). The decorrelation time scales inversely with the baseline length and could reach an hour for the shortest baselines and large primary beams, in agreement with Figure 1. A notable feature of Figure 2 is the alignment of the isocontours of decorrelation time. Its shape is determined by the interplay of decorrelation owing to the rotation and the traversal of the intensity pattern and can be derived analytically.

For large primary beams, the decorrelation time is $\simeq 1/(|\mathbf{u}_0|\Omega_{0g}^{1/2}|\sin\phi|)$ (point (b), (Eq. (23)); the decorrelation profile for large primary beams is seen to follow this function. For small primary beams, the decorrelation time is $\simeq \Omega_{0g}^{1/2}/\cos\phi$, nearly independent of the length of the baseline (point (a)). Equating these two expressions gives us: $\Omega_{0g}|\tan\phi||\mathbf{u}_0| \simeq 1$. This relation is shown in Figure 2 (White line) and it separates the regions dominated by decorrelation owing to the rotation (above the White line) from the regions in which the translation plays the dominant role. Figure 2 shows the White line adequately captures the essential physics of the separation of the two regions. We note that the large field of view (point (c) above) does not play an important role in our study because of the range of telescope latitudes we consider, which is motivated by the location of radio interferometers studied here. For $\phi \simeq 90^\circ$, both translation and large field of view effects are negligible while, for $\phi \simeq 0$, the impact of rotation is negligible while translation and wide field of view effects dominate (Eq. (23)).

2.1.2. The phase of visibility correlation function

In the foregoing we studied the amplitude of the correlation function. As the correlation function (in either frequency or delay space Eq. (9) or Eq. (15)) is a complex function we need to know the correlation properties of its phase in addition to complete the analysis.

In Appendix B, we discuss how suitable approximations allow us to discern major contributors to the phase of the correlation function. Eqs. (B7) and (B8) show that the phase angle is $2\pi u_0 \cos\phi\Delta H + \psi_1 + \psi_2$. The term $2\pi u_0 \cos\phi\Delta H$ has already been discussed above (point (a) on traversal time of coherence scale). It follows from Eq. (B8) that both ψ_1 and ψ_2 are small as compared to $2\pi u_0 \cos\phi\Delta H$ as $\psi_1 \propto \Omega_g$ and $\psi_2 \propto \Omega_g^2$ for $\pi^2\Omega_g^2 y^2 < 1$. ψ_2 can only be significant when effects arising from large field-of-view become important (Eq. (B8) and discussion on point (c) above), which is not the case for $w_0 = 0$ and the primary beams we consider in our analysis. The dominant phase angle $2\pi u_0 \cos\phi\Delta H$ can be explicitly identified in Eq. (B7) in this case.

Motivated by our analytic results, we define the phase angle as:

$$\psi(\mathbf{u}, t' - t) = \text{Arg} \left(\exp(-i2\pi u_0 \cos\phi\Delta H) \left\langle V_\tau(\mathbf{u}_0, w_0, t) V_\tau^*(\mathbf{u}_0, w_0, t') \right\rangle \right) \quad (24)$$

The multiplication by the additional phase allows for near cancellation of the phase term $\exp(ik_{\perp 1} r_0 \cos\phi\Delta H)$ in Eq. (15) (or a similar term in Eq. (9) for correlation in frequency space if u_0 and r_0 are replaced by u_ν and r_ν , respectively). In Figure 3 we present our numerical results. We notice that the phase angle defined by Eq. (24) is small for a wide range of Δt , as suggested by our analytic results. This means, as anticipated, that the phase of the correlation function is nearly $\exp(i2\pi u_0 \cos\phi\Delta H)$ ⁵. The implication of this result for drift scan data analysis will be discussed below.

2.2. Approximations and input quantities

Our results use an input HI power spectrum, different primary beams, and a set of approximations to transform from frequency to delay space. We discuss the impact of these approximations and input physics on our analysis.

2.2.1. Dependence on input power spectrum and the shape of primary beam

⁵ The origin of this phase can partly be explained by considering a simpler case: a single point source of flux F_ν at the phase center. In this case, the visibility $V_\nu(\mathbf{u}) = F_\nu A_\nu(0)$, where $A_\nu(0)$ defines the primary beam response at the phase center, $l = 0$ and $m = 0$. The correlation between visibilities separated by ΔH in time in a drift scan is $V_\nu(\mathbf{u})V_\nu^*(\mathbf{u}) \simeq F_\nu^2 A_\nu^2(0) \exp(i2\pi u_\nu \cos\phi\Delta H)$. As discussed in section 3.1 the same factor scales out of the correlation function for a set of point sources also.

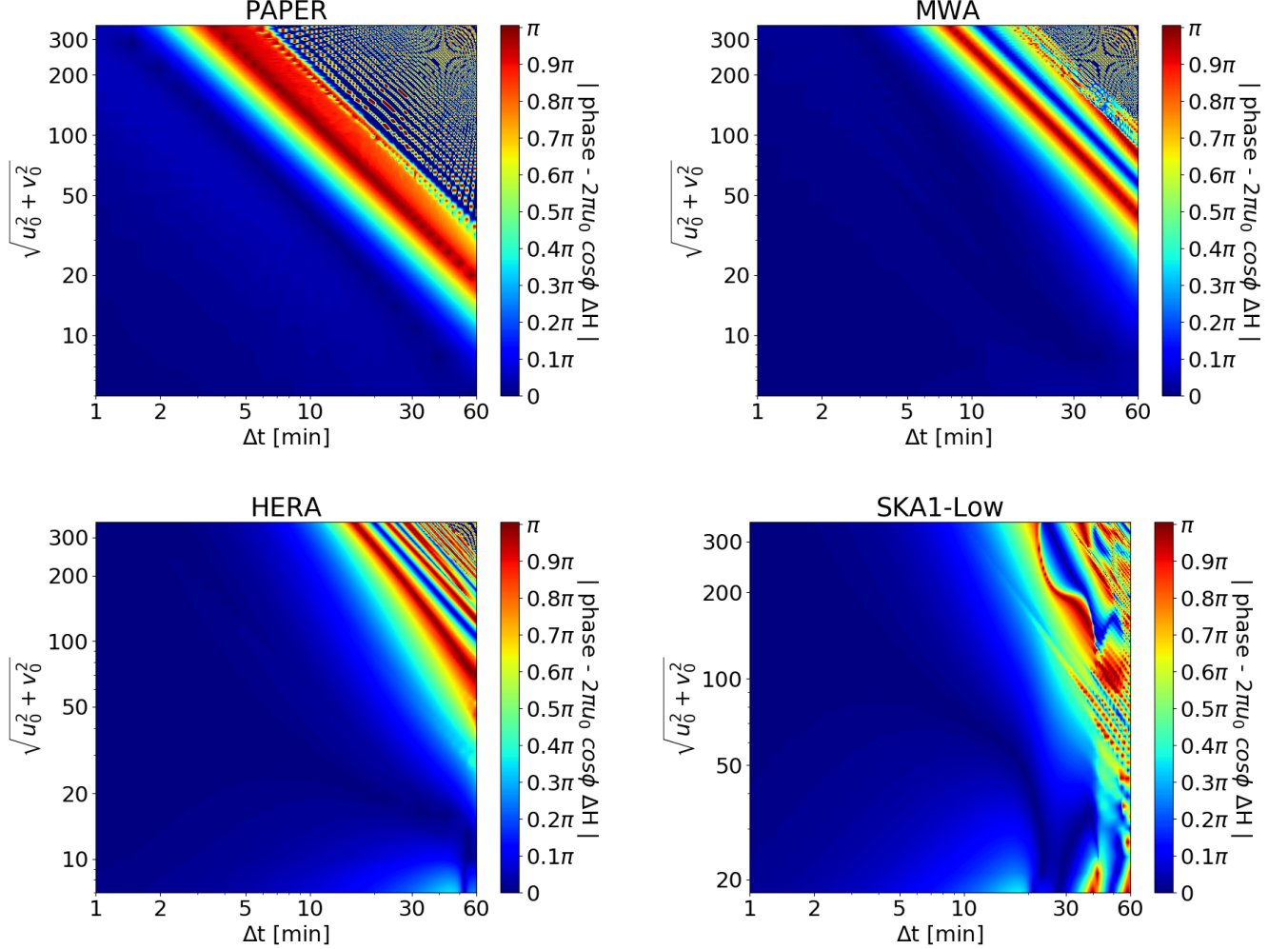


Figure 3. The figure shows the absolute value of the phase angle of the visibility correlation function (Eq. (24)) as a function of $\Delta t = t' - t$. This figure illustrates that the rapidly fluctuating component of the phase of the complex correlation function (Eq. (18)) can mostly be removed by multiplying it with $\exp(-i2\pi u_0 \cos \phi \Delta H)$. This allows us to determine the time scales for averaging the time-ordered visibilities in drift scans (section 2.1.2 and 4).

The results shown in Figure 1 were derived using the HI power spectrum, $P(k) \simeq 1/k^n$, with $n \simeq 2$, for a range of scales (Furlanetto et al. 2006). We tested our results with different power-law HI power spectra with spectral indices in the range $n = 1-3$ and found our results to be insensitive to the input power spectra.

The lack of dependence of the visibility decorrelation time on the input HI power spectrum follows from our analysis. Eqs. (B6) and (B7) show that relevant approximations allow us to separate the input power spectrum from the time-dependent part of the correlation function, which means Figure 1 is independent of the HI power spectrum. These equations show that the time dependence of the correlation function is essentially captured by the response of the primary beam in Fourier space. Similar expression was derived in Parsons et al. (2016) (their equation 9) for cases when the Fourier beam (Eq. (10)) has a narrow response (e.g. PAPER).

The only cases not covered by this approximation are small primary beams and small baselines. However, for the limiting cases we discuss here, $|\mathbf{u}| \gtrsim 20$ and SKA1-Low primary beam, our numerical results show that the impact of the input HI power spectrum on the decorrelation time scale is negligible.

Our results are insensitive to the shape of the primary beam. We compare our numerical results for instrumental primary beams with a symmetric, separable Gaussian beam by roughly matching Ω_{0g} and the main lobe of the instrumental primary beam. We find excellent agreement in explaining the main features of Figures 1, 2 and 3. Eq. (B7) adequately explains Figure 1, except for small baselines for HERA and SKA1-Low.

2.2.2. Approximations in transforming from frequency to delay space

Following Eq. (15) we discuss various approximations used in making the correlation function in delay space more tractable. In the tracking case, these approximations allow us to find a one-to-one linear relation between the Fourier modes of the HI signal with the variables of radio interferometers (e.g. Paul et al. 2016 and references therein). However, owing to the frequency dependence of the primary beam, the coordinate distance, and the baseline, these commonly-used relations are approximate. We assessed the impact of these approximations in Paul et al. (2016) for the tracking case. For a bandwidth $B = 10$ MHz ($\nu_0 = 154$ MHz) and MWA primary beam, the error in these relations is less than 5% for $k_{\parallel} \gtrsim 0.1 \text{ Mpc}^{-1}$. The modes corresponding to $k_{\parallel} \lesssim 0.1 \text{ Mpc}^{-1}$ are buried in the foreground wedge and therefore do not play a role in the detection of the HI signal (e.g. Paul et al. 2016). The error increases with bandwidth and primary beam and therefore is expected to be smaller for HERA and SKA1-Low for the same bandwidth. As we also use these approximations in our work to separate the variables on the sky-plane from those along the line-of-sight, we re-assess these approximations for a drift scan and find these errors to be of similar magnitude for the drift scan. As in the tracking case, these approximations allow us to derive the relation between baseline and delay space parameter τ and Fourier modes of the HI signal. This simplification allows us to write the frequency-dependent terms in the form expressed in Eq. (16).

One outcome of this approximation for drift scans is that the functional form of the decorrelation time shown in Figure 1 is nearly the same in frequency and delay space. Therefore, Figure 1 can be interpreted as displaying the decorrelation time at the center of the bandpass. This assertion is borne out by Eq. (B6).

Our study is based on the assumption $\nu_0 \simeq 154 \text{ MHz}$ and $B \simeq 10 \text{ MHz}$. It can readily be extended to a different frequency/bandpass by using Eqs. (B6) and/or (B7).

We discuss the approximation in transforming from frequency to delay space further with regard to foregrounds and the analysis of drift scan data in later sections (see footnote 6).

It is worthwhile to reiterate the scope of the main approximations we use: (a) For large primary beams and baselines, Eq. (B6) provides an excellent approximation, (b) for small bandwidths and primary beams, Eq. (B6) can readily be extended to Eq. (B7), (c) for small baselines and primary beams, Eq. (B6) might not be valid and Eq. (18) has to be computed numerically.

3. FOREGROUNDS IN DRIFT SCANS

In the tracking mode, the foregrounds can be isolated from the HI signal ('EoR window') by transforming to delay space if the two-dimensional foregrounds are spectrally smooth and therefore their correlation scales differ from the three-dimensional HI signal along the line of sight. However, in tracking mode, we cannot use the difference between correlation properties of foregrounds and the HI signal on the sky plane. In a drift scan, it is possible that the decorrelation time of the HI signal is different from components of foregrounds, which might give us yet another way to mitigate foregrounds.

The aim of this section is to study the decorrelation time scales of two components of foregrounds: near-isotropic distribution of point sources of flux above 1 Jy and statistically homogeneous and isotropic diffuse foregrounds. In our analysis, the delay space approach continues to be the primary method used to isolate foregrounds from the HI signal and we therefore present all our results in this space.

3.1. Point Sources

In a drift scan the phase center is held fixed while the intensity pattern changes. The changing intensity pattern owing to a set of point sources can be written as:

$$I_{\nu}(\boldsymbol{\theta}, t) = \sum_m F_{\nu}^m \delta^2(\boldsymbol{\theta} - \boldsymbol{\theta}_m(t)) \quad (25)$$

Here F_{ν}^m is the flux of the m^{th} source and $\boldsymbol{\theta}_m(t)$ its angular position at time t . Here all the angles are measured with respect to the phase center which is assumed to be fixed at $\boldsymbol{\theta}_0 = 0$. The visibility (retaining the w -term) can readily be derived from the expression above:

$$V_{\nu}(\mathbf{u}_{\nu}, w_{\nu}, t) = \sum_m F_{\nu}^m A_{\nu}(\boldsymbol{\theta}_m(t)) \exp[-2\pi i (\mathbf{u}_{\nu} \cdot \boldsymbol{\theta}_m(t) + w_{\nu}(n_m(t) - 1))] \quad (26)$$

To discern the main results of this section, we ignore the frequency dependence of source fluxes and primary beam, even though we allow these quantities to be frequency dependent in our simulations⁶. Using Eq. (14) the visibility of point sources in the delay space is:

$$V_\tau(\mathbf{u}_0, w_0, t) \simeq \sum_m F_0^m A_0(\boldsymbol{\theta}_m(t)) B \text{sinc}(\pi B \bar{\tau}^m(t)) e^{2\pi i \nu_0 \bar{\tau}^m(t)} \quad (27)$$

$$\text{where,} \quad \bar{\tau}^m(t) = \tau - \frac{1}{\nu_0} (\mathbf{u}_0 \cdot \boldsymbol{\theta}_m(t) + w_0(n_m(t) - 1)) \quad (28)$$

The correlation function of the visibilities in delay space can be written as:

$$\begin{aligned} \langle V_\tau(\mathbf{u}_0, w_0, t) V_\tau^*(\mathbf{u}_0, w_0, t') \rangle &\simeq B^2 \sum_m \sum_n F_0^m F_0^n A_0(\boldsymbol{\theta}_m(t)) A_0(\boldsymbol{\theta}_n(t')) \\ &\times \text{sinc}(\pi B \bar{\tau}^m(t)) \text{sinc}(\pi B \bar{\tau}^n(t')) e^{2\pi i \nu_0 (\bar{\tau}^m(t) - \bar{\tau}^n(t'))} \end{aligned} \quad (29)$$

Here the ensemble average implies averages over all pairs of baselines and times for which $|\mathbf{u}_0|$ and $t' - t$ are held fixed. To understand Eq. (29) we first consider the tracking case in which source positions are independent of time. In this case the dominant contribution comes from $\tau = 2\pi \mathbf{u}_0 \cdot \boldsymbol{\theta}_m / \nu_0$. This defines the so-called foreground wedge which is bounded by the maximum value of θ_m which is given approximately by the size of the primary beam. It also follows from the equation that the sum is dominated by terms for which $m = n$.

In a drift scan the source position changes with respect to the primary beam. It means the value of τ for which the sum in Eq. (29) peaks changes with time. While the broad wedge structure is the same in this case as in the tracking case as the dominant contribution comes from sources within the primary beam, the correlation structure becomes more complicated. As $\boldsymbol{\theta}_n(t') - \boldsymbol{\theta}_m(t)$ remains unchanged during a drift scan, the summation in this case would also generally be dominated by $m = n$ terms. However, it is possible that a source at one position at a time drifts close to the position of another source at another time. Even though the contribution of this pair could be negligible in tracking mode, it would not be if the visibilities are correlated at two different times. The impact of this effect requires details of point source distribution which we model using a simulation in this paper.

For the case of $m = n$, the same source is correlated at two different times. In this case, it follows from Eq. (29) that the visibility correlation diminishes as the time separation increases. As the additional time-dependent phase acquired in the drift is proportional to the length of the baseline, the decorrelation time scale is expected to be shorter for longer baselines.

Point source simulations: We generate 15067 point sources brighter than 1 Jy distributed isotropically on the southern hemisphere (Hopkins et al. 2003). We assume the spectral index of sources to be -0.7 ⁷. For this source distribution we compute the power spectrum in delay space as a function of drift time. In a drift scan, the coordinates of these sources evolve according to Eq. (A2) with respect to the fixed phase center.

We compute visibilities in delay space for a one-hour drift scan. The visibilities are then correlated in time and the visibility correlation function is computed by averaging over the number of correlation pairs for which $t' - t$ and $|\mathbf{u}_0|$ are held fixed:

$$\langle V_\tau(\mathbf{u}_0, w_0, t) V_\tau^*(\mathbf{u}'_0, w'_0, t') \rangle = \frac{1}{N_{|\mathbf{u}_0|}} \sum_{|\mathbf{u}_0|} \frac{1}{N_{tt'}} \sum_{t, t'} V_\tau(\mathbf{u}_0, w_0, t) V_\tau^*(\mathbf{u}'_0, w'_0, t') \quad (30)$$

Here $N_{|\mathbf{u}_0|}$ and $N_{tt'}$ are the number of baseline pairs for fixed $|\mathbf{u}_0|$ and $t - t'$, respectively.

To establish how the amplitude of the visibility correlation behaves as a function of time, baselines, and the number of points over which the average is computed, we choose two representative baselines $|\mathbf{u}_0| = 20, 100$. We carry out averages in a ring of width $\Delta|\mathbf{u}_0| = 4$; each of these rings is populated, randomly and uniformly, with $N_{|\mathbf{u}_0|} = 25, 50, 100, 200, 400$.

⁶ We neglect the frequency dependence of the intensity pattern and the primary beam throughout this paper. As we compare our analytic results against simulations in this section, it allows us to verify this assumption more explicitly. We find this assumption to be extremely good for bandwidth $B \simeq 10$ MHz around a central frequency of $\nu_0 \simeq 154$ MHz. This approximation can be understood by considering a simpler case: a flat spectrum source at the phase center. While transforming to delay space, this source receives contribution from only the $\tau = 0$ mode. If the source is now assumed to have a spectral index, more delay space modes close to $\tau = 0$ begin to contribute. We find that these modes do not contaminate the EoR window as they lie well within the wedge given the bandwidth and spectral index of interest. The leakage into the EoR window owing to finite bandwidth can be assuaged by using a frequency-space convolving function such as Blackman-Nuttall window or a Gaussian window we discuss in the section on diffuse foregrounds. The frequency dependence of baselines in the phase plays a more important role and is needed to explain the wedge structure for foregrounds (e.g. Paul et al. 2016).

⁷ Foreground components from both the point sources and diffuse galactic emission are expected to be dominated by synchrotron radiation from power-law energy distribution of relativistic electrons. The galaxy is optically thin to these photons, therefore, the observed spectrum retains the form of the emitted spectrum, which is featureless. The main mechanism of the absorption of radio photons in the interstellar medium is free-free absorption off thermal and non-thermal electrons. The optical depth of free-free absorption: $\tau = 3.3 \times 10^{-7} (T/10^4)^{-1.35} \nu^{-2.1} \text{EM}$, where ν is in GHz and EM, the emission measure, is observationally determined to be: $\text{EM} = 5 \text{ pc cm}^{-3}$ (e.g. Haffner et al. 1999); the optical depth is negligible at frequencies of interest to us.

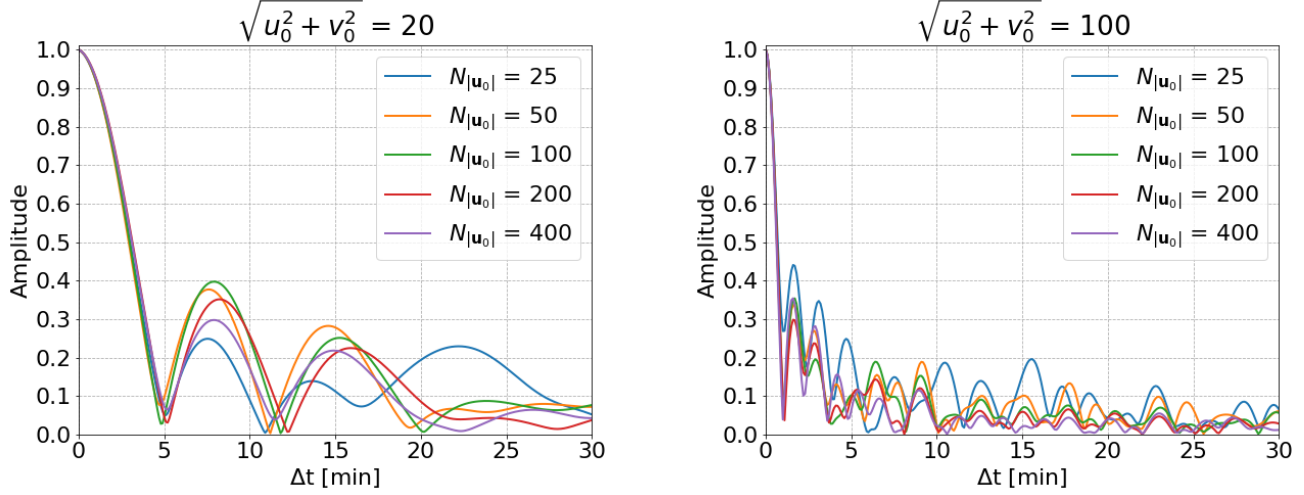


Figure 4. The visibility correlation function (Eq. (30)) is shown as a function of Δt (normalized to unity for $\Delta t = 0$) for two baselines $\sqrt{u_0^2 + v_0^2} = 20, 100$ for $u_0 = v_0$, for MWA primary beam and latitude. The visibility correlation function is seen to fall to half its value in a few minutes.

In Figure 4, the visibility correlation functions are plotted for the two cases using the instrumental parameters of MWA (primary beam and ϕ) for $\tau = 0$ and $w_0 = 0$. We notice the following: (a) averaging over more baselines causes the correlation function to decorrelate faster when the number of baselines are small but the function converges as the number of baselines is increased, (b) the correlation function decorrelates faster for larger baselines, as anticipated earlier in the section based on the analytic expression, Eq. (29), (c) a comparison between Figures 4 and 1 shows the decorrelation time scale for the HI signal is much larger than for a set of point sources. For $|\mathbf{u}_0| = 100$, the point sources decorrelate to 50% of the peak in less than a minute while this time is nearly 10 minutes for the HI signal.

The structure of the foreground wedge in a drift scan is expected to be similar to the tracking mode; we verify it using analytic estimates and simulations but do not show it here.

3.2. Diffuse correlated foregrounds

An important contribution to the foregrounds comes from diffuse galactic emission (DGE) which is correlated on the sky plane; this component of the foregrounds is dominated by optically-thin galactic synchrotron emission. The spatial and frequency dependence of this emission is separable if the emission is optically thin, which, as noted above, is a good assumption and is key to the separation of foregrounds from the HI signal. We consider statistically homogeneous and isotropic component of the diffuse foreground here. This case differs from the HI signal only in different frequency dependencies of the two signals. Therefore, the formulation is similar to the case of HI signal discussed above.

As we assume the DGE to be statistically homogeneous and isotropic, the two-point function of fluctuations on the plane of the sky in Fourier space could be characterized by a power spectrum C_q such that and $q = |\mathbf{q}| = \sqrt{q_1^2 + q_2^2}$, where $\mathbf{q} = (q_1, q_2)$, with q_1 and q_2 being the two Fourier components on the sky plane. C_q can be expressed as:

$$\langle I_\nu(\mathbf{q}) I_{\nu'}(\mathbf{q}') \rangle = (2\pi)^2 C_q(\nu, \nu') \delta^2(\mathbf{q} - \mathbf{q}') \quad (31)$$

For our analysis we adopt the following form and normalization of C_q , as appropriate for $\nu \simeq 150$ (e.g. Ghosh et al. (2012) and references therein):

$$C_q(\nu, \nu') = a_0 \left(\frac{\nu}{\nu_0} \right)^{-\alpha} \left(\frac{\nu'}{\nu_0} \right)^{-\alpha} \left(\frac{q}{1000} \right)^{-\gamma} \quad (32)$$

where $\alpha = 0.52$ (Rogers & Bowman 2008) is the spectral index and $\gamma = 2.34$ (Ghosh et al. 2012) is the index of spatial power spectrum. The value of $a_0 = A_0 (2k_B \nu_0^2 / c^2)^2$ is 237 Jy^2 at $\nu_0 = 154 \text{ MHz}$. It rescales the amplitude factor, $A_0 = 513 \text{ mK}^2$, given in Ghosh et al. (2012) from $(\text{mK})^2$ at 150 MHz to Jy^2 at ν_0 . For a single polarization this factor should be divided by 4.

Using the formalism used for analysing the HI signal it can readily be shown that the visibility correlation function in frequency space can be related to C_q as:

$$\left\langle V_\nu(\mathbf{u}_\nu, w_\nu, t) V_\nu^*(\mathbf{u}'_\nu, w'_\nu, t') \right\rangle = \int \frac{d^2 q}{(2\pi)^2} C_q(\nu, \nu') e^{iq_1 \cos \phi \Delta H} Q_\nu(\mathbf{q}, \mathbf{u}_\nu, w_\nu, \Delta H = 0) Q_\nu^*(\mathbf{q}, \mathbf{u}'_\nu, w'_\nu, \Delta H) \quad (33)$$

where the Fourier beam of DGE is:

$$Q_\nu(\mathbf{q}, \mathbf{u}_\nu, w_\nu, \Delta H) = \int d^2 \theta A_\nu(\boldsymbol{\theta}) \exp \left[-2\pi i \left(\mathbf{x}_u \cdot \boldsymbol{\theta} - \frac{1}{2} y \theta^2 \right) \right] \quad (34)$$

$$\text{with} \quad x_u = u_\nu - \frac{1}{2\pi} (q_1 + q_2 \sin \phi \Delta H) \quad (35)$$

$$x_v = v_\nu - \frac{1}{2\pi} (q_2 - q_1 \sin \phi \Delta H) \quad (36)$$

$$y = w_\nu + \frac{1}{2\pi} q_1 \cos \phi \Delta H \quad (37)$$

In Eq. (34) we have used Q -integrals (or 2D Fourier beam) defined for the HI correlation function (Eq. (10)). Comparing Eq. (34) and Eq. (10) we note that the following relation between the Fourier modes of correlated diffuse foregrounds and the HI signal: $\mathbf{q} \simeq r_0 \mathbf{k}_\perp$.

As already shown for the HI signal, Eq. (34) can be made more tractable by assuming the primary beam to be separable and symmetric. To establish general characteristics of DGE foreground we carry out analytical calculations with a symmetric Gaussian beam: $e^{-(l^2+m^2)/\Omega_g}$, which allows us to extend the integration limits from $-\infty$ to $+\infty$. Following the HI analysis, we also expand n to the first order. This gives us:

$$Q_\nu(\mathbf{q}, \mathbf{u}_\nu, w_\nu, \Delta H) = \pi \Omega'_g \exp \left[-\pi^2 \Omega'_g (x_u^2 + x_v^2) \right] \quad (38)$$

where $\Omega'_g = \Omega_g / (1 - i\pi y \Omega_g)$. It should be noted that these variables can be read off directly from Q -integrals defined for the HI signal by putting $r_0 \mathbf{k}_\perp \simeq \mathbf{q}$. This shows the equivalence of the HI signal and diffuse foregrounds in the Fourier domain on the plane of the sky.

We next carry out frequency integrals to transform to delay space. As already discussed in section 3.1, the main results in the delay space can be obtained by retaining only the frequency dependence of baselines because the foregrounds wedge in the two-dimensional power spectrum of foregrounds arises largely due to the chromaticity of baselines (e.g. Paul et al. 2016).

The frequency integral can be computed numerically for a finite bandpass. To carry out analytical calculations, the limits of the frequency integral can be extended to infinity. However, under this assumption, the baseline ($\mathbf{u}_\nu = \mathbf{u}_0 \nu / \nu_0$) also becomes infinity and the integral does not converge⁸. To correctly pick the relevant scales of diffuse foregrounds, we apply a Gaussian window function in frequency space ($\exp(-c_2(\nu - \nu_0)^2)$) which allows us to pick the relevant scales within the bandwidth (B) of the instrument and also enables us to extend the limits of integration.⁹ This gives us:

$$\begin{aligned} \tilde{Q}(\mathbf{q}, \mathbf{u}_0, w_0, \Delta H) &= \int_{\nu_0 - B/2}^{\nu_0 + B/2} d\nu e^{2\pi i \tau \nu} e^{-c_2(\nu - \nu_0)^2} Q_\nu(\mathbf{q}, \mathbf{u}_\nu, w_\nu, \Delta H) \\ &= \pi \Omega'_g \sqrt{\frac{\pi}{c_1 + c_2}} \exp \left[-\frac{\pi^2 \tau^2}{c_1 + c_2} \right] \exp \left[2\pi i \tau \nu_0 \left(1 + \frac{c_1}{c_1 + c_2} \frac{1}{|\mathbf{q}_u|} (a_1 + a_2 \sin \phi \Delta H) \right) \right] \\ &\quad \times \exp \left[-\frac{\Omega'_g}{4} \left(\frac{c_2}{c_1 + c_2} (a_1 + a_2 \sin \phi \Delta H)^2 + (a_2 - a_1 \sin \phi \Delta H - |\mathbf{q}_u| \sin \phi \Delta H)^2 \right) \right] \end{aligned} \quad (39)$$

where $c_1 = (|\mathbf{q}_u|/\nu_0)^2 \Omega'_g/4$, $c_2 = 1/(bB^2)$, $\mathbf{q}_u = 2\pi \mathbf{u}_0$, $a_1 = q_1 - 2\pi u_0$, $a_2 = q_2 - 2\pi v_0$. The parameter b is a numerical factor which can be tuned to get the desired width of the Gaussian window function. The argument of the factor $\exp[-2\pi^2 \tau^2 / (c_1 + c_2)]$ in Eq. (39) yields the linear relation corresponding to the foreground wedge.

⁸ This highlights the main difference between the HI signal and the two-dimensional diffuse foregrounds. In the former, the frequency integral picks the scale along the line-of-sight k_\parallel while no such scale exists for diffuse foregrounds

⁹ A similar window (e.g. Blackman-Nuttall window, e.g. Paul et al. 2016) is applied to the data to prevent the leakage of foregrounds from the foreground wedge to the clean EoR window.

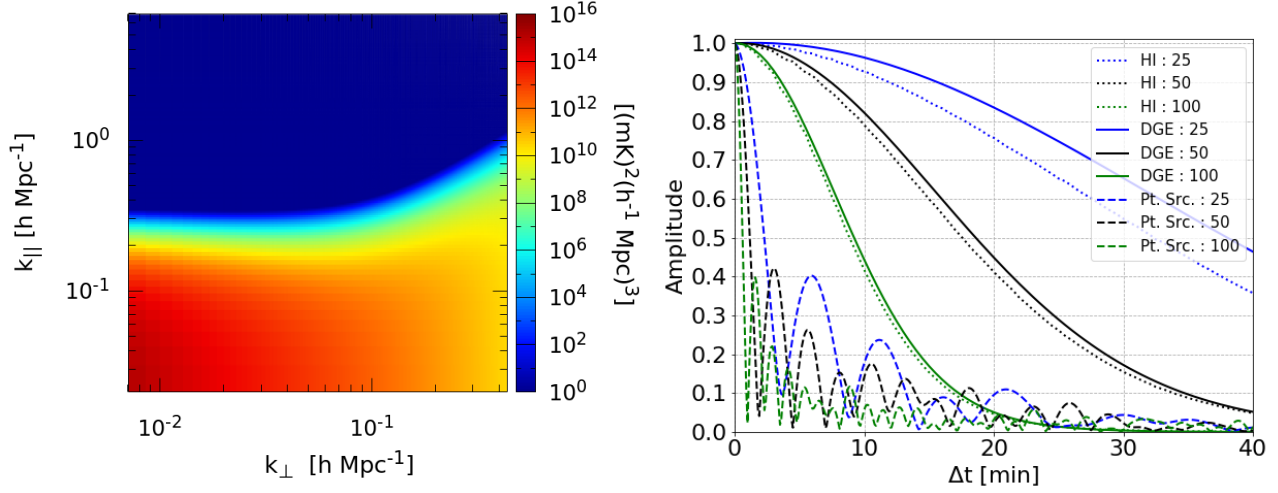


Figure 5. In the left panel, we show two-dimensional power spectrum of DGE ($\Delta H = 0$) in the k_{\parallel} - k_{\perp} plane in units $(\text{mK})^2(\text{h}^{-1}\text{Mpc})^3$. The figure assumes $\nu_0 = 154$ MHz and bandwidth $B = 10$ MHz. The relation applicable to the HI signal is used to transform from the telescope variables (u_0, v_0, τ) to the Fourier modes $(\mathbf{k}_{\perp}, k_{\parallel})$, and to convert the power spectrum to the appropriate units (e.g. Paul et al. 2016). The Figure highlights the separation of foregrounds from the EoR window; the bandwidth determines the extent of the flat region parallel to the k_{\parallel} axis. In the right panel, the visibility correlation function (normalized to unity for $\Delta t = 0$) for DGE is shown for three baselines $\sqrt{u_0^2 + v_0^2} = 25, 50, 100$ (Eq. (40)). We also show the HI and point source visibility correlation functions for comparison.

We can read off the correlation scales for diffuse correlation foregrounds from Eq. (39). A baseline \mathbf{u}_0 is most sensitive to the Fourier mode $\mathbf{q}_{\mathbf{u}}$. As in the case of the HI signal, the decorrelation time scale for a drift scan can be estimated readily by putting $\mathbf{q} = \mathbf{q}_{\mathbf{u}}$ and simplifying the expression. We finally obtain:

$$\begin{aligned} \langle V_{\tau}(\mathbf{u}_0, w_0, t) V_{\tau}^*(\mathbf{u}'_0, w'_0, t') \rangle &= \iint_{\nu_0 - B/2}^{\nu_0 + B/2} d\nu d\nu' \langle V_{\nu}(\mathbf{u}_{\nu}, w_{\nu}, t) V_{\nu'}^*(\mathbf{u}'_{\nu'}, w'_{\nu'}, t') \rangle \\ &= \int \frac{d^2 q}{(2\pi)^2} C_q(\nu_0, \nu_0) e^{i q_1 \cos \phi \Delta H} \tilde{Q}(\mathbf{q}, \mathbf{u}_0, \Delta H = 0) \tilde{Q}^*(\mathbf{q}, \mathbf{u}'_0, \Delta H) \end{aligned} \quad (40)$$

Eq. (40) gives the general expression for visibility correlation function in delay space for a drift scan observation. It can be computed by using Eqs. (32), (39) in Eq. (40). It reduces to the relevant expression for tracking observation for $\Delta H = 0$. In Figure 5 we show numerical results obtained from solving Eq. (40) for a Gaussian primary beam matched to the main lobe of MWA primary beam and $\phi = -26.7^\circ$. We display the power spectrum in k_{\parallel} - k_{\perp} plane for $\Delta H = 0$ and the correlation of diffuse correlated foregrounds as a function of time. Our main conclusions are:

1. Like the point sources, diffuse correlated foregrounds are confined to a wedge and the EoR window is clean for the detection of the HI signal.
2. The diffuse foregrounds decorrelate on time scales comparable to the HI signal. (We note that the difference between the two cases for the shortest baseline is partly because we use the exact MWA beam for the HI case while we use the Gaussian beam for diffuse foreground.) This should be contrasted with point-source foregrounds that decorrelate on a much shorter time scale as compared to the HI signal.

4. ANALYSING DRIFT SCAN DATA

Our study allows us to address the following question: over what time period can the time-ordered visibility data be averaged without diminishing the HI signal. We further seek optimal signal-to-noise for the detection of the HI signal. We computed two-point visibility correlation function to assess the coherence time scale of visibilities. Our results are shown in Figures 1–2 (amplitude of the correlation function as a function of Δt , baseline and primary beam) and 3 (the

phase of the complex correlation function). Our study shows that the range of time scales over which time-ordered visibilities can be averaged without the loss of HI signal lies in the range of a few minutes to around 20 minutes.

Motivated by our theoretical analysis, we define the quantity:

$$\mathcal{C}_\tau(\mathbf{u}_0, w_0, t' - t) \equiv \exp(-i2\pi u_0 \cos \phi \Delta H) \langle V_\tau(\mathbf{u}_0, w_0, t) V_\tau^*(\mathbf{u}_0, w_0, t') \rangle \quad (41)$$

Notice that $\mathcal{C}_\tau(\mathbf{u}_0, w_0, t' - t) = \mathcal{C}_\tau^*(\mathbf{u}_0, w_0, t - t')$. Our analysis shows that the complex number $\mathcal{C}_\tau(\mathbf{u}_0, w_0, t' - t)$ is dominated by its real component with a phase which remains small over the coherence time scale of the amplitude (Figure 3 and Figure 2). Our aim is to extract $\mathcal{C}_\tau(\mathbf{u}_0, w_0, t' - t)$ from the data and then suitably weigh it to extract the HI signal, optimally and without the loss of HI signal¹⁰. We discuss two possible ways to extract the HI signal. The first is based on averaging the visibilities before computing the correlation function.

We consider visibilities measured with time resolution ΔH (ΔH is assumed to be much smaller than the coherence scale of visibilities for any baseline of interest to us, e.g. $\Delta H = 10$ sec). Let us denote the measured visibilities as, V_n , where n corresponds to the time stamp; each visibility is a function of baseline and either ν or τ . As noted above, we could use data in either frequency or delay space. For the discussion here, we consider delay space and express all quantities as functions of ν_0 . For brevity, we only retain the time dependence of measured visibilities. We define:

$$\mathcal{V} = \sum_{n=1}^N \exp(i2\pi u_0 \cos \phi \Delta H n) V_n \quad (42)$$

The total time of over which the visibilities are averaged $T = N\Delta H$ should be small enough such that the signal decorrelation is negligible (Figure 1). For instance, we could choose N such that the decorrelation is 0.9, which corresponds roughly to 10 minutes for MWA for $\sqrt{u_0^2 + v_0^2} \simeq 20$. It also follows that if the visibilities are averaged for a period much longer than the correlation scale of the signal, there would be serious loss of the HI signal. Even though we define \mathcal{V} for a single baseline \mathbf{u}_0 , it can also be obtained by averaging visibilities over all redundant baselines. The correlation function that extracts the HI signal $|\langle V_\tau(\mathbf{u}_0, w_0, t) V_\tau^*(\mathbf{u}_0, w_0, t') \rangle|$ then is:

$$\mathcal{C}_{\text{HI}} \simeq \frac{1}{N^2} \mathcal{V} \mathcal{V}^* \quad (43)$$

Notice that \mathcal{C}_{HI} is nearly the same as the expression in Eq. (41) in this case. A longer stream of data of length, $K \gg N$, can be divided into time slices of $N\Delta H$. The correlation function can be estimated for each slice using this method (coherent averaging as the number of pairs is $\simeq N^2$) and then averaged further over different time slices (incoherent averaging over K/N slices). \mathcal{C}_{HI} is also optimal as the noise RMS is nearly the same for each pair of correlated visibilities. We note that the HI signal is mostly contained in the real part of this resulting function, as the phase angle is small for time scales over which the visibilities are averaged (Figure 3).

A much better method to utilize the functional form shown in Figure 1 is to use the estimator:

$$\mathcal{C}_{\text{HI}} \simeq \frac{1}{N^2} \sum_{n'} \sum_n \exp(-i2\pi u_0 \cos \phi \Delta H (n' - n)) V_n V_{n'}^* g^{-1}(n' - n) \quad (44)$$

Here $g(n' - n)$ corresponds to the time decorrelation function shown in Figure 1; by construction, $g(n' - n)$ is real, $g(n - n) = 1$, and $g(n' - n) = g(n - n')$. The difference between this approach and the first method is that visibilities are correlated first and then averaged. This yields the same final expression as the first method if $g(n' - n)$ is applied for a suitable time interval such that it is close to unity. A distinct advantage of this method is that we could only retain cross-correlations such that $n' \neq n$, which allows us to avoid self-correlation or noise bias; the total number of cross-correlations are $\simeq N^2/2$ in this case. This estimator is unbiased with respect to the detection of HI signal but does not minimize noise RMS. The following estimator is both unbiased and optimal:

$$\mathcal{C}_{\text{HI}} = \frac{\sum_{n'} \sum_n \exp(-i2\pi u_0 \cos \phi \Delta H (n' - n)) V_n V_{n'}^* g(n' - n)}{\sum_{n'} \sum_n g^2(n' - n)} \quad (45)$$

¹⁰ To prevent HI signal loss, the simplest way to extract the HI signal from drift scans would be to not use the coherence of visibilities in time. Assuming visibilities are measured with time resolution much shorter than the coherence time scale, visibilities with identical time stamps can be squared (after averaging over redundant baselines) to compute the power spectrum. This gives an unbiased estimator of the HI signal. However, in such a procedure, visibilities measured at two different times are treated as uncorrelated which results in an estimator with higher noise as compared to what is achievable using further information regarding coherence of visibilities in time. If the time resolution of visibilities is around 10 seconds and the coherence time is around 10 minutes, then the noise RMS of the visibility correlation is higher by roughly the square root of the ratio of these two times.

The estimator is unbiased for any choice of $g(n' - n)$. However, for using this estimator, small values of $g(n' - n)$ (e.g. $g(n' - n) < 0.3$) should be avoided to prevent averaging over very noisy visibility pairs. As in the first method, the real part of this function dominates the HI signal.

The amplitude of C_{HI} for both the proposed estimators extracts the visibility correlation function at equal time, $\langle V_{\tau}(\mathbf{u}_0, w_0, t) V_{\tau}^*(\mathbf{u}_0, w_0, t) \rangle$, which is real. The estimation of HI power spectrum from this function has been extensively studied in the analysis of EoR tracking data (e.g. Paul et al. 2016).

Our method has similarities with other approaches proposed to analyze the drift scan data. In Parsons et al. (2016), the fringe-rate filters have been applied on the visibility data. We apply a similar filter to reduce rapid oscillations of the phase of the correlation function. We note that the filter applied in Parsons et al. (2016) takes into all the components of earth's rotation (Eq. (A4)). In our analysis, we identify the different roles played by these components. We show how the components responsible for the rotation and translation of the intensity pattern cause the decorrelation of the amplitude of the correlation function while the component that gives rise to the translation dominates the phase of the correlation function. In m -mode analysis (Shaw et al. (2014, 2015)) the intensity pattern is expanded using spherical harmonics and the time variation of the intensity pattern is solely owing to the change in the azimuthal angle ϕ . This time variation can then be Fourier transformed to extract m -modes of the data. The filter we apply in Eq. (42) corresponds to a similar process. Eq. (42) can be viewed as a Fourier transform in which a single mode is extracted for a time-window of the duration given roughly by the decorrelation time of the amplitude of the correlation function. Our analysis shows that such a procedure, directly applied on measured visibilities, can extract the relevant information of the HI signal.

4.1. Impact on foregrounds

The measured visibilities are a linear sum of the HI signal, foregrounds, and the noise, which are uncorrelated with each other. In this paper, we also compute the time scale of the decorrelation of a set of point source and statistically-homogeneous and isotropic diffuse foregrounds. Does our method allow us to mitigate foregrounds?

First, we notice that the phase factor $\exp(-i2\pi \cos \phi u_0 \Delta H)$ we apply to curtail rapid oscillations of the correlation function of the HI signal has the same form for foregrounds (Eqs. (33) and (29)). Hence, it doesn't play a role in separating foregrounds from the HI signal.

However, the decorrelation time scale of point sources is smaller than the HI signal. In this case, the following situation is possible: two visibilities separated in time are correlated such that the HI component is fully extracted ($g(n' - n) = 1$) but the point source component is uncorrelated. This means that there would be partial decorrelation of this component of foregrounds when either of the two methods discussed above are used to extract the HI signal. But this argument doesn't apply to diffuse foregrounds.

Therefore, it is possible to partly reduce the level of foregrounds in a drift scan but the primary method of separating foregrounds from the HI signal remains transforming to delay space, as in a tracking observation.

5. SUMMARY AND CONCLUSION

In this paper we address the following question: over what time scales are time-ordered visibilities coherent in a drift scan for the EoR HI signal, set of point sources, and diffuse correlated foregrounds. This is an extension of our earlier work (Paul et al. 2014) and has similarities with other approaches in the literature (Shaw et al. 2014; Parsons et al. 2016). Our main theoretical tool is the complex two-point correlation function of visibilities measured at different times. We consider the primary beams of PAPER, MWA, HERA, and SKA1-Low for our analysis. Our main results can be summarized as:

- Figure 1 shows the amplitude of the correlation function of HI visibilities in time for four interferometers. The correlation time scales vary from a few minutes to nearly 20 minutes for the cases considered. We identify the three most important factors that cause decorrelation: (a) traversal time across a coherent feature, (b) rotation of sky intensity pattern, and (c) large field of view.
- The time variation of the phase of the HI correlation function is dominated by a filter function which is determinable in terms of measurable quantities (component of east-west baseline, latitude of the telescope, etc.). This filter function can be absorbed into an overall phase. The phase angle of the resultant function is small, which means the complex correlation function is dominated by its real part. The phase angle remains small over the coherence time scale of the amplitude of the correlation function (Figure 3).

- Our results are valid in both frequency and delay space and are insensitive to the input HI power spectrum. By implication they are directly applicable to the analysis of EoR drift scan data.
- The nature of foregrounds in a drift scan is different from the tracking mode owing to the time dependence of the sky intensity pattern. We consider two components of foregrounds for our analysis: set of point sources and statistically homogeneous diffuse correlated emission. The decorrelation time scales for these components are displayed in Figures 4 and 5. The point sources decorrelate faster than the HI signal. This provides a novel way to partly mitigate foregrounds using only information on the sky plane. However, the diffuse foreground decorrelation time scale is comparable to that of the HI signal and the contamination from this component cannot be removed in a drift scan on the sky plane. By implication, the delay space formalism remains the principal method for isolating foregrounds from the HI signal (Figure 5).

We discuss in detail how our formalism can be used to extract the HI signal from the drift scan data. We argue many different approaches might be possible for the lossless retrieval of the HI signal while optimizing the noise. In the future, we hope to apply our formalism to publicly-available drift scan data.

APPENDIX

A. COORDINATE TRANSFORMATION

Here we discuss sky coordinate system (l, m, n) in terms of (δ, ϕ, H) with δ, ϕ, H representing the declination, the terrestrial latitude of the telescope, and the hour angle, respectively. From Eq. (A4.7) of [Christiansen & Hoegbom \(1969\)](#):

$$\begin{aligned} l &= \cos \delta \sin H \\ m &= \cos \delta \cos H \sin \phi - \sin \delta \cos \phi \\ n &= \cos \delta \cos H \cos \phi + \sin \delta \sin \phi \end{aligned} \quad (\text{A1})$$

In a drift scan, the primary beam remains unchanged with respect to a fixed phase center chosen to be $l = m = 0$. The coordinates of intensity pattern (l, m, n) change with time, in the first order in ΔH , as:

$$\begin{aligned} \Delta l &= (m \sin \phi + n \cos \phi) \Delta H \\ \Delta m &= -l \sin \phi \Delta H \\ \Delta n &= -l \cos \phi \Delta H \end{aligned} \quad (\text{A2})$$

The change in hour angle, ΔH , can be expressed in terms of radians as:

$$\Delta H[\text{in rad}] = \frac{\pi}{12} \frac{\Delta t[\text{in min}]}{60} \quad (\text{A3})$$

We use Eq. (A2) to express the time-dependent part of Eq. (9) explicitly in terms of change in hour angle ΔH . Eq. (A3) can be used to express ΔH in terms of drift time Δt for a zenith scan.

$$\begin{aligned} -\frac{r_0}{2\pi} \mathbf{k}_\perp \cdot \Delta \boldsymbol{\vartheta}(\Delta t) &= -\frac{r_0}{2\pi} (k_{\perp 1} \Delta l + k_{\perp 2} \Delta m) \\ &= -\frac{r_0}{2\pi} (k_{\perp 1} (m \sin \phi + n \cos \phi) \Delta H - k_{\perp 2} l \sin \phi \Delta H) \\ &\simeq -\frac{r_0}{2\pi} (k_{\perp 1} \cos \phi \Delta H + (-l k_{\perp 2} + m k_{\perp 1}) \sin \phi \Delta H) + \frac{1}{2} (l^2 + m^2) \frac{r_0}{2\pi} k_{\perp 1} \cos \phi \Delta H \end{aligned} \quad (\text{A4})$$

We use the flat-sky approximation $n \simeq 1 - \frac{1}{2} (l^2 + m^2)$ in writing Eq. (A4).

B. FURTHER SIMPLIFICATION OF VISIBILITY CORRELATION FUNCTION

In this appendix we discuss how the visibility correlation function can be further simplified for large primary beams and long baselines. This allows us to discern several generic properties of the correlation function. We start with the HI visibility correlation function in frequency space (Eq. (9)):

$$\begin{aligned} \left\langle V_\nu(\mathbf{u}_\nu, w_\nu, t) V_\nu^*(\mathbf{u}'_{\nu'}, w'_{\nu'}, t') \right\rangle &= \bar{I}_\nu \bar{I}_{\nu'} \int \frac{d^3 k}{(2\pi)^3} P_{HI}(k) e^{ik_\parallel |\dot{r}_0| \Delta \nu} \\ &\quad e^{ir_\nu k_{\perp 1} \cos \phi \Delta H} Q_\nu(\mathbf{k}_\perp, \mathbf{u}_\nu, w_\nu, \Delta H = 0) Q_{\nu'}^*(\mathbf{k}_\perp, \mathbf{u}'_{\nu'}, w'_{\nu'}, \Delta H) \end{aligned}$$

The Fourier beam can be expressed as (Eq. (10)):

$$Q_\nu(\mathbf{k}_\perp, \mathbf{u}_\nu, w_\nu, \Delta H) = \int d^2\theta A_\nu(\boldsymbol{\theta}) \exp \left[-2\pi i \left(\mathbf{x}_u \cdot \boldsymbol{\theta} - \frac{1}{2} y \theta^2 \right) \right] \quad (\text{B5})$$

with

$$\begin{aligned} x_u &= u_\nu - \frac{r_\nu}{2\pi} (k_{\perp 1} + k_{\perp 2} \sin \phi \Delta H) \\ x_v &= v_\nu - \frac{r_\nu}{2\pi} (k_{\perp 2} - k_{\perp 1} \sin \phi \Delta H) \\ y &= w_\nu + \frac{r_\nu}{2\pi} k_{\perp 1} \cos \phi \Delta H \end{aligned}$$

We consider a Gaussian beam: $A(l, m) = e^{-(l^2+m^2)/\Omega_g}$ to compute the Fourier beam:

$$Q_\nu(\mathbf{k}_\perp, \mathbf{u}_\nu, w_\nu, \Delta H) = Q(x_u, x_v, y) = \frac{\pi \Omega_g}{1 - i\pi y \Omega_g} \exp \left[-\frac{\pi^2 \Omega_g (x_u^2 + x_v^2)}{1 - i\pi y \Omega_g} \right]$$

For $\Omega'_g \equiv \Omega_g / (1 - i\pi y \Omega_g)$

$$Q_\nu(\mathbf{k}_\perp, \mathbf{u}_\nu, w_\nu, \Delta H) = Q(x_u, x_v, y) = \pi \Omega'_g \exp \left[-\pi^2 \Omega'_g (x_u^2 + x_v^2) \right]$$

If Ω_g is large, e.g. PAPER or MWA beams, we can use δ -function approximation for solving $Q_\nu(\mathbf{k}_\perp, \mathbf{u}_\nu, w_\nu, \Delta H = 0)$, which gives us:

$$\begin{aligned} Q_\nu(\mathbf{k}_\perp, \mathbf{u}_\nu, w_\nu, \Delta H = 0) &= \delta \left(u_\nu - \frac{r_\nu}{2\pi} k_{\perp 1} \right) \delta \left(v_\nu - \frac{r_\nu}{2\pi} k_{\perp 2} \right) \\ Q_\nu(\mathbf{k}_\perp, \mathbf{u}_\nu, w_\nu, \Delta H = 0) &= \left(\frac{2\pi}{r_\nu} \right)^2 \delta^2 \left(\mathbf{k}_\perp - \frac{2\pi}{r_\nu} \mathbf{u}_\nu \right) \end{aligned}$$

This allows us to express HI visibility correlation function in frequency space as:

$$\begin{aligned} \left\langle V_\nu(\mathbf{u}_\nu, w_\nu, t) V_{\nu'}^*(\mathbf{u}'_{\nu'}, w'_{\nu'}, t') \right\rangle &= \frac{\bar{I}_\nu \bar{I}_{\nu'}}{r_\nu^2} e^{2\pi i u_\nu \cos \phi \Delta H} Q_{\nu'}^*(\mathbf{k}_\perp, \mathbf{u}'_{\nu'}, w'_{\nu'}, \Delta H) \\ &\quad \int \frac{dk_\parallel}{2\pi} P_{HI}(k) e^{ik_\parallel |\dot{r}_0| \Delta \nu} \end{aligned} \quad (\text{B6})$$

In the previous equation we have used, $\mathbf{k}_\perp = 2\pi \mathbf{u}_\nu / r_\nu$. Eq. (B6) gives an excellent approximation for MWA and PAPER, and for HERA and SKA1-Low for long baselines in frequency space. This can be readily be computed at any frequency and explains the features seen in Figure 1.

We can extend our analysis to HI visibility correlation function in delay space (Eq. (15)):

$$\left\langle V_\tau(\mathbf{u}_0, w_0, t) V_\tau^*(\mathbf{u}'_0, w'_0, t') \right\rangle = \iint_{\nu_0 - B/2}^{\nu_0 + B/2} d\nu d\nu' \left\langle V_\nu(\mathbf{u}_\nu, w_\nu, t) V_{\nu'}^*(\mathbf{u}'_{\nu'}, w'_{\nu'}, t') \right\rangle e^{-2\pi i \tau \Delta \nu}$$

Here B is the observational bandwidth. We make the same approximations discussed in section 2.1, which gives us:

$$\begin{aligned} \left\langle V_\tau(\mathbf{u}_0, w_0, t) V_\tau^*(\mathbf{u}'_0, w'_0, t') \right\rangle &= \frac{\bar{I}_0^2}{r_0^2} e^{2\pi i u_0 \cos \phi \Delta H} Q_{\nu_0}^*(\mathbf{k}_\perp, \mathbf{u}'_0, w'_0, \Delta H) \\ &\quad \int \frac{dk_\parallel}{2\pi} P_{HI}(k) \int \int_{\nu_0 - B/2}^{\nu_0 + B/2} d\nu d\nu' e^{i\Delta \nu (k_\parallel |\dot{r}_0| - 2\pi \tau)} \\ \left\langle V_\tau(\mathbf{u}_0, w_0, t) V_\tau^*(\mathbf{u}'_0, w'_0, t') \right\rangle &\simeq \frac{\bar{I}_0^2}{r_0^2} e^{2\pi i u_0 \cos \phi \Delta H} Q_{\nu_0}^*(\mathbf{k}_\perp, \mathbf{u}'_0, w'_0, \Delta H) \\ &\quad \int \frac{dk_\parallel}{2\pi} P_{HI}(k) \frac{2\pi B}{|\dot{r}_0|} \delta \left(k_\parallel - \frac{2\pi \tau}{|\dot{r}_0|} \right) \end{aligned}$$

In deriving this equation, we use the following result from section 2.1:

$$\iint_{\nu_0-B/2}^{\nu_0+B/2} d\nu d\nu' e^{i\Delta\nu(k_{\parallel}|\dot{r}_0|-2\pi\tau)} = B^2 \text{sinc}^2 \left[\pi B \left(\tau - \frac{|\dot{r}_0|}{2\pi} k_{\parallel} \right) \right] \simeq \frac{2\pi B}{|\dot{r}_0|} \delta \left(k_{\parallel} - \frac{2\pi\tau}{|\dot{r}_0|} \right)$$

The HI signal is strongly correlated when $|\mathbf{u}_0 - \mathbf{u}'_0| \lesssim 2/\Omega_g^{1/2}$, which allows us to use $\mathbf{u}'_0 \approx \mathbf{u}_0$. This gives us:

$$\left\langle V_{\tau}(\mathbf{u}_0, w_0, t) V_{\tau}^*(\mathbf{u}'_0, w'_0, t') \right\rangle \simeq \frac{\bar{I}_0^2 B}{r_0^2 |\dot{r}_0|} e^{2\pi i u_0 \cos \phi \Delta H} Q_{\nu_0}^*(\mathbf{k}_{\perp}, \mathbf{u}_0, w'_0, \Delta H) P_{HI}(k) \quad (\text{B7})$$

where $k = \sqrt{(2\pi\tau/|\dot{r}_0|)^2 + (2\pi u_0/r_0)^2 + (2\pi v_0/r_0)^2}$. Though Eq. (B7) was derived using a Gaussian beam, it is in excellent agreement with the numerical results for MWA and PAPER and for HERA and SKA1-Low for longer baselines ($|\mathbf{u}| \gtrsim 150$) shown in Figure 1. Eq. (B7) also shows that the decorrelation time is expected to be nearly independent of the delay parameter τ .

We next give explicit forms of the amplitude and the phase of the Fourier beam. We have:

$$Q_{\nu}(\mathbf{k}_{\perp}, \mathbf{u}_{\nu}, w_{\nu}, \Delta H) = Q(x_u, x_v, y) = \frac{\pi\Omega_g}{1 - i\pi y\Omega_g} \exp \left[-\frac{\pi^2\Omega_g(x_u^2 + x_v^2)}{1 - i\pi y\Omega_g} \right]$$

where $x_u^2 + x_v^2 = |\mathbf{u}_{\nu}|^2 \sin^2 \phi \Delta H^2$ and $y = w_{\nu} + u_{\nu} \cos \phi \Delta H$. Then,

$$\begin{aligned} Q_{\nu}(\mathbf{k}_{\perp}, \mathbf{u}_{\nu}, w_{\nu}, \Delta H) &= \pi z_1 z_2 = \pi a_1 e^{i\psi_1} a_2 e^{i\psi_2} = \pi a_1 a_2 e^{i(\psi_1 + \psi_2)} \\ \text{Amp}[Q_{\nu}(\mathbf{k}_{\perp}, \mathbf{u}_{\nu}, w_{\nu}, \Delta H)] &= \pi a_1 a_2 \\ \text{Arg}[Q_{\nu}(\mathbf{k}_{\perp}, \mathbf{u}_{\nu}, w_{\nu}, \Delta H)] &= \psi_1 + \psi_2 \\ z_1 &= a_1 e^{i\psi_1} = \frac{\Omega_g}{1 - i\pi y\Omega_g} \\ z_2 &= a_2 e^{i\psi_2} = \exp \left[-\frac{\pi^2\Omega_g(x_u^2 + x_v^2)}{1 - i\pi y\Omega_g} \right] \end{aligned}$$

On solving a_1, ψ_1, a_2, ψ_2 in terms of known quantities, we find;

$$\begin{aligned} a_1 &= \frac{\Omega_g}{\sqrt{1 + \pi^2\Omega_g^2 y^2}} \\ \psi_1 &= \arctan(\pi\Omega_g y) \\ a_2 &= \exp \left[-\pi^2(x_u^2 + x_v^2) a_1 \cos \psi_1 \right] = \exp \left[-\pi^2(x_u^2 + x_v^2) \frac{\Omega_g}{1 + \pi^2\Omega_g^2 y^2} \right] \\ \psi_2 &= -\pi^2(x_u^2 + x_v^2) a_1 \sin \psi_1 = -\pi^2(x_u^2 + x_v^2) \frac{\Omega_g}{1 + \pi^2\Omega_g^2 y^2} (\pi\Omega_g y) \end{aligned}$$

Hence,

$$\begin{aligned} \text{Amp}[Q_{\nu}(\mathbf{k}_{\perp}, \mathbf{u}_{\nu}, w_{\nu}, \Delta H)] &= \pi a_1 a_2 = \frac{\pi\Omega_g}{\sqrt{1 + \pi^2\Omega_g^2 y^2}} \exp \left[-\pi^2(x_u^2 + x_v^2) \frac{\Omega_g}{1 + \pi^2\Omega_g^2 y^2} \right] \\ \text{Arg}[Q_{\nu}(\mathbf{k}_{\perp}, \mathbf{u}_{\nu}, w_{\nu}, \Delta H)] &= \psi_1 + \psi_2 = \arctan(\pi\Omega_g y) - \pi^2(x_u^2 + x_v^2) \frac{\Omega_g}{1 + \pi^2\Omega_g^2 y^2} (\pi\Omega_g y) \quad (\text{B8}) \end{aligned}$$

The total phase acquired by the HI visibility correlation function is $2\pi u_0 \cos \phi \Delta H + \psi_1 + \psi_2$.

REFERENCES

Ali, Z. S., Parsons, A. R., Zheng, H., et al. 2015, ApJ, 809, —. 2018, ApJ, 863, 201

- Barry, N., Wilensky, M., Trott, C. M., et al. 2019, arXiv e-prints, arXiv:1909.00561
- Beardsley, A. P., Hazelton, B. J., Sullivan, I. S., et al. 2016, ArXiv e-prints, arXiv:1608.06281
- Bowman, J. D., Cairns, I., Kaplan, D. L., et al. 2013, PASA, 30, 31
- Bowman, J. D., Rogers, A. E. E., Monsalve, R. A., Mozdzen, T. J., & Mahesh, N. 2018, *Nature*, 555, 67
- Cheng, C., Parsons, A. R., Kolopanis, M., et al. 2018, *ApJ*, 868, 26
- Choudhuri, S., Bharadwaj, S., Chatterjee, S., et al. 2016, *MNRAS*, 463, 4093
- Christiansen, W. N., & Hoegbom, J. A. 1969, *Radiotelescopes*
- Cornwell, T. J., Golap, K., & Bhatnagar, S. 2008, *IEEE Journal of Selected Topics in Signal Processing*, 2, 647
- Datta, A., Bowman, J. D., & Carilli, C. L. 2010, *ApJ*, 724, 526
- DeBoer, D. R., Parsons, A. R., Aguirre, J. E., et al. 2017, *PASP*, 129, 045001
- Dillon, J. S., Neben, A. R., Hewitt, J. N., et al. 2015, *PhRvD*, 91, 123011
- Eastwood, M. W., Anderson, M. M., Monroe, R. M., et al. 2018, *AJ*, 156, 32
- Fan, X., Strauss, M. A., Becker, R. H., et al. 2006, *AJ*, 132, 117
- Furlanetto, S. R., Oh, S. P., & Briggs, F. H. 2006, *PhR*, 433, 181
- Ghosh, A., Prasad, J., Bharadwaj, S., Ali, S. S., & Chengalur, J. N. 2012, *MNRAS*, 426, 3295
- Haffner, L. M., Reynolds, R. J., & Tufte, S. L. 1999, *ApJ*, 523, 223
- Hopkins, A. M., Afonso, J., Chan, B., et al. 2003, *AJ*, 125, 465
- Kolopanis, M., Jacobs, D. C., Cheng, C., et al. 2019, arXiv e-prints, arXiv:1909.02085
- Lanman, A. E., & Pober, J. C. 2019, *MNRAS*, 487, 5840
- Morales, M. F., & Wyithe, J. S. B. 2010, *ARA&A*, 48, 127
- Paciga, G., Chang, T.-C., Gupta, Y., et al. 2011, *MNRAS*, 413, 1174
- Parsons, A. R., & Backer, D. C. 2009, *AJ*, 138, 219
- Parsons, A. R., Liu, A., Ali, Z. S., & Cheng, C. 2016, *ApJ*, 820, 51
- Parsons, A. R., Pober, J. C., Aguirre, J. E., et al. 2012, *ApJ*, 756, 165
- Parsons, A. R., Liu, A., Aguirre, J. E., et al. 2014, *ApJ*, 788, 106
- Patil, A. H., Yatawatta, S., Koopmans, L. V. E., et al. 2017, *ApJ*, 838, 65
- Paul, S., Sethi, S. K., Subrahmanyam, R., et al. 2014, *ApJ*, 793, 28
- Paul, S., Sethi, S. K., Morales, M. F., et al. 2016, *ApJ*, 833, 213
- Planck Collaboration, Ade, P. A. R., Aghanim, N., et al. 2016, *A&A*, 594, A13
- Planck Collaboration, Aghanim, N., Akrami, Y., et al. 2018, ArXiv e-prints, arXiv:1807.06209
- Pritchard, J. R., & Loeb, A. 2012, *Reports on Progress in Physics*, 75, 086901
- Rogers, A. E. E., & Bowman, J. D. 2008, *AJ*, 136, 641
- Shaw, J. R., Sigurdson, K., Pen, U.-L., Stebbins, A., & Sitwell, M. 2014, *ApJ*, 781, 57
- Shaw, J. R., Sigurdson, K., Sitwell, M., Stebbins, A., & Pen, U.-L. 2015, *PhRvD*, 91, 083514
- Singh, S., Subrahmanyam, R., Shankar, N. U., et al. 2018, *Experimental Astronomy*, 45, 269
- Taylor, G. B., Carilli, C. L., & Perley, R. A., eds. 1999, *Astronomical Society of the Pacific Conference Series*, Vol. 180, *Synthesis Imaging in Radio Astronomy II*
- Tingay, S. J., Goeke, R., Bowman, J. D., Emrich, D., & others. 2013, *PASA*, 30, 7
- Trott, C. M. 2014, *PASA*, 31, e026
- Trott, C. M., Pindor, B., Procopio, P., et al. 2016, *ApJ*, 818, 139
- van Haarlem, M. P., Wise, M. W., Gunst, A. W., et al. 2013, *A&A*, 556, A2
- Wayth, R. B., Tingay, S. J., Trott, C. M., et al. 2018, ArXiv e-prints, arXiv:1809.06466